Spring 7-1-2017

MICRODISCHARGES UTILIZED IN PORTABLE GAS SENSING AND THEIR ATMOSPHERIC CONTAMINANTS

Colin H. Sillerud
University of New Mexico

Colin H. Sillerud

Chemical and Biological Engineering

This thesis is approved, and it is acceptable in quality and form for publication

Approved by the Thesis Committee

Dr. Elizabeth L. Dirk , Chairperson

Dr. Sang M. Han

Dr. Ronald P. Manginell

MICRODISCHARGES UTILIZED IN PORTABLE GAS SENSING AND THEIR ATMOSPHERIC CONTAMINANTS

By

COLIN H. SILLERUD

B.S. CHEMICAL ENGINEERING, UNIVERSITY OF NEW MEXICO

THESIS

Submitted in Partial Fulfillment of the Requirements for the Degree of

Masters of Science
Chemical Engineering

University of New Mexico
Albuquerque, New Mexico

July 2017

ACKNOWLEDGMENTS

I acknowledge Dr. Ronald Manginell, my research advisor at Sandia National Laboratories (SNL), for the opportunity to pursue my master's degree and for his faith in my ability to accomplish the goals he set forth. Though my faith in myself wavered at times, his incredible financial, intellectual and emotional support keep pushing me to be the best that I could be. I will carry his friendship and guidance throughout my life in matters both professional and personal.

I thank Dr. Elizabeth Hedberg-Dirk, my committee chair, for her expert instruction, both during my undergraduate career and as my master's advisor at the University of New Mexico. Her wealth of life experience proved invaluable in the ups as well as the downs.

Thank you to Dr. Sang M. Han for his tremendous lecturing and expectations of excellence in the classroom.

I will forever be indebted to my experimental advisor, Dr. Peter Schwindt, for his depth of knowledge on electric systems and physics, as well as for his compassion and understanding.

My group members at SNL – Dr. Ben T. Yee, Dr. Joe Simonson, Mathew Moorman, John Anderson, and Nathaniel Pfiefer – were the foundation from which I stood. Their experience, knowledge and guidance are represented throughout the following work.

I would further like to thank Dr. Douglas Read, my first mentor at SNL, for giving me the chance to explore my talents and the freedom to make mistakes. His mentorship and friendship will be treasured.

Additional thanks to Dr. Juan Elizondo-Decanini for high-speed circuit design, Kathy Myers for device packaging and wirebonding, Dr. Matt Hopkins and Dr. Andy Fierro for

discussions on plasma theory and pulsing techniques, Dr. Todd Barrick for vacuum equipment installation, Al Staton for hardware installation, and Dr. Wahid Hermina, Dr. Steve Casalnuovo, Mary Crawford, and the LDRD office for their gracious operational and financial contributions.

I also express my deep gratitude to my friends throughout Albuquerque and the world for their support, encouragement, and laughter.

Lastly, I would be nowhere without the support and encouragement of my family and girlfriend. As a result, I dedicate this work to my mother, Dr. Karen R. Halliday, my father, Dr. Laurel O. Sillerud, my brother, Timothy H. Sillerud, and my girlfriend, Meredith Brunet-Lecomte. They both awakened my passions for knowledge of the world and supported my explorations of life. I only hope to continue to meet their expectations.

Microdischarges Utilized In Portable Gas Sensing And Their Atmospheric Contaminants

By

Colin H. Sillerud

M.S., Chemical Engineering, University of New Mexico, 2017

ABSTRACT

Portable applications of microdischarges such as the chemical detection, remediation of gaseous wastes, or the destruction of volatile organic compounds will mandate operation in the presence of contaminant species. This work examines the temporal evolution of microdischarge optical and ultraviolet emissions during pulsed operation by experimental methods. By varying the pulse length of a microdischarge initiated in a 4-hole silicon microcavity array operating in a 655 Torr ambient primarily composed of Ne, we were able to measure the emission growth rates for different contaminant species native to the discharge environment as a function of pulse length. It was found that emission from hydrogen and oxygen impurities demonstrated similar rates of change, while emissions from molecular and atomic nitrogen, measured at 337.1 nm and 120 nm respectively, exhibited the lowest rate of change. We conclude that it is likely that O_2 undergoes the same resonant energy transfer process between rare gas excimers that has been shown for H_2. Further, efficient resonant processes were found to be favored during ignition and

extinction phases of the pulse, while emission at the 337.1 nm line from N_2 was favored during the intermediate stage of the plasma. In addition to experimental results, a zero-dimensional analysis is also presented to further understand the nature of the microdischarge.

Table of Contents

List of Figures

List of Tables

Chapter 1

Microdischarges as Excitation Sources for Chemical Detectors

1.1. Introduction

More than one person dies each day due to preventable chemical exposure in the United States [5]. Globally, more than 350,000 people die each year from unintentional chemical poisoning [10]. Further, in the current global terrorism climate, chemical attacks like those in the Tokyo subway system in 1998 as well as those by ISIS and al-Qaeda over the last twenty years have become increasingly likely [11].

The detection of hazardous chemicals utilizes three types of devices classified as: 1) field-portable [1], 2) field deployable, and 3) field collection with laboratory analysis [12]. Field-portable devices can be easily carried and allow for on-site sample analysis. Field-deployable devices are installed on-site and offer autonomous operation including data collection and analysis for extended periods. The last method, field collection followed by off-site laboratory analysis, is the most comprehensive, universal and specific in its results, but it is time consuming and so it is used primarily for analysis after an event. To provide actionable information that can save lives during an event, field analysis is required. Though field-ready systems are being produced [1], many factors have slowed their widespread adoption including field contamination, high power consumption, and sensor fouling to name a few.

Chemical detection systems are comprised of three main components: the pre-concentrator, the column, and the detector. First, the pre-concentrator, which serves as a sample amplifier, adsorbs the sample onto a suitable material until it is released as a plug, often via thermal ramp [13, 14]. Second, the plug flows into the column coated with a stationary phase, which retards the flow of analytes based on their interaction with the phase [15, 16]. Third, the separated analytes flow to the detector, which typically gives the retention time of each species. By comparing the retention time of each species to that of a known sample, the identity of the

unknown samples can be determined. This work will focus on the third stage of the system, the detector. Power supply, gas supply, chemical handling, ease of use, and contamination are critical concerns with any portable detector.

1.2. Detectors for Chemical Sensing

Detectors for gas chromatography (GC) fall into two general classifications: universal and selective. While universal detectors often examine bulk properties such as thermal conductivity and are widely applicable, they can suffer from poor selectivity and are easily affected by changes to external factors such as temperature [17, 18]. Selective detectors, on the other hand, react to specific properties of analytes and not the carrier gas [6]. Examples include flame ionization detectors (FIDs), electron capture detectors (ECDs), chemiresistors, photoionization detectors (PIDs), and mass spectrometers (MS).

The FID is the most widely used detector in conventional GC due to its high sensitivity (*pg* for hydrocarbons) and ease of use. However, FIDs require gas supplies such a H_2 and suffer from a dramatic reduction in their sensitivity with respect to non-carbon based compounds. Further, the signal output of a FID is directly proportional to its size, so smaller sensors suffer from a loss in signal [19]. Absorptive sensors such as chemiresistors typically feature response times > 1 s and can be poisoned by solvents [20, 21]. Fabry-Perot type detectors have low detection levels, but require high-energy input due to their utilization of lasers, beam splitter/collimators, and spectrometer/photodetectors [22, 23]. Mass spectrometers are often referred to as the ‘gold standard’ of analytical techniques, but they have prohibitive size, vacuum and operational gas needs [24].

As recently as 2012, peer researchers have expressed a need for improved detection capabilities [25]. This detector should meet four requirements: 1) low limits of detection, 2) low operational power consumption, 3) simple and inexpensive fabrication, 4) non-destructive and non-selective for analytes [6]. The micro-discharge (plasma) based photoionization detector has been shown to meet these requirements [6].

1.2.1. The Photoionization Detector

The photoionization detector (PID) provides a portable and stable detector with relatively low power consumption, making it a reasonable choice for field use [1, 12]. PIDs use photons from a plasma source to excite and disassociate electrons from their corresponding analyte molecules. The ionized molecules are attracted to the cathode and registered as an increase in current on the order of (pA). As shown in Figure 1-1, they are constructed using a plasma source, a window, an analyte flow channel and a charged electron collector. The excitation of the analyte is predicated on the energy of the photon and the analyte's ionization potential (I.P.). This is a non-destructive process that allows for further sample analysis by downstream detection. Further, PIDs do not use combustible make-up gases such as H_2, so they are safe for use in environments where combustion could be hazardous.

The gas-phase ionization of a neutral molecule, M, is assumed to proceed through the stepwise path of: direct photon impact, excitation, and ionization shown in Eq. (1).

$$M + h\nu \rightarrow M^* \rightarrow M^+ + e^- \quad (1)$$

However, many competing relaxation pathways exist, including, but not limited to, the loss of product ions (M^+) via electron recapture and neutralizing collisions with other molecules such as

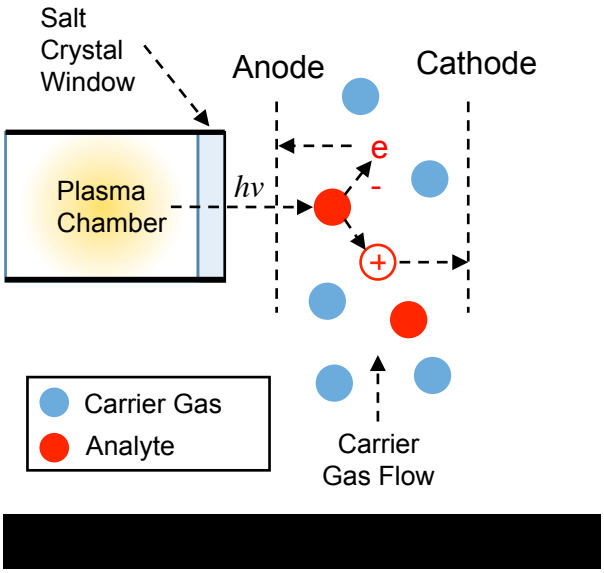

contaminants and gas carrier molecules. These competing pathways reduce the detector signal response and lessen the detector efficiency. In the ideal case, under conditions of little or no competing reactions with impurities, the following equation (Eq. 2) describes detector response:

$$i = IF\eta\sigma NL[\mathrm{M}] \qquad (2)$$

where i is the detector current, I is the initial photon flux, F is the faraday constant, η is the photoionization efficiency, σ is the molecule's absorption cross-section, N is Avogadro's number, L is the path length of the excited molecule, and [M] is the molecule's gas concentration [26].

The range of analytes that can be detected by a PID is a function of the energy of the photons delivered, which is a function of the PID's constituent gases and the transmittance of the window. Table 1-1 shows the strongest lines produced by available VUV lamps. The current limit of detection is the Argon lamp with a lithium fluoride window, which reaches energies of 11.83 eV (104.8 nm). However, this is a limit on the range of analytes that a PID with a window can detect.

Nominal Lamp Photon Energies	Fill Gas	Major Emission Lines (eV)	Major Emission Lines (nm)	Relative Intensity	Window Crystal	Crystal Transmittance λ Range (nm) **
11.7-11.8	Ar	11.83	104.8	1000	LiF	105-5000
		11.62	106.7	500		
10.6	Kr	10.64	116.5	200	MgF_2	115-7000
		10.03	123.6	650		
10.2	H_2	10.2	121.6	1000	MgF_2	
		10.2	121.6	500		
9.8-10.0	Kr	10.03	123.6	650	CaF_2	125-8000
9.5-9.6	Xe	9.92	125	250	BaF_2	135-9900
		9.57	129.6	1000		
		8.44	147	600		
9.5	O_2	9.52	130.2	900	CaF_2	
		9.5	130.5	600		
		9.49	130.6	300		
8.4	Xe	8.44	147	600	Al_2O_3	145-4500
					SiO_2	145-2300

The window grants certain benefits as well as drawbacks. Using different gas and window configurations, PIDs gain high selectivity in certain cases by operating in between the ionization potentials of different analytes. For example, aromatic compounds (I.E. ~ 8-9 eV) can

be selectively detected amongst a background of alkanes (I.E. ~ 10-13 eV) by using a Xe lamp with a BaF_2 window (9.5 eV) [27]. However, many analytes of interest have a higher IP than the LiF window will transmit (11.83 eV). Some examples include, Freon (IP: 11.77 to 12.91 eV), methane (IP: 12.98 eV), and chlorine trifluride (IP: 12.65 eV) [28].

Removal of the window in certain designs, allows for detection of basically any analyte. Common configurations rely on a simple rod-shaped electrode structure to generate the DC-powered glow discharge [9, 29]. Helium is the gas of choice for windowless atomic emission spectroscopy due to its ionization (24.58 eV) and excitation energies (19.82, 20.62 eV), and for photoionization due to photon energies ranging from 13.5 to 17.5 [30], which are the highest of all elements. This allows He PIDs (HPID) to excite and ionize any element [31, 32].

1.2.2. Microdischarges in Chemical Detection

Microdischarges (MD) offer a potential step towards realizing the potential of the PID as a field detector. The term microdischarge, though it is not clearly defined, refers to a non-local thermal equilibrium (non-LTE) plasma whose small dimensions lead to new physical properties [33] such as an increased power density, high excimer concentrations [34], and the predominance of plasma sheaths. Types of MDs include, direct current (DC), capacitive coupled discharges (CCD), inductively coupled discharges (ICD), microwave induced discharges (MID), radio frequency induced discharges (rfID), micro hollow cathode discharges (MHCD), and dielectric barrier discharges (DBD) [35].

MDs couple the efficient generation of UV and VUV emissions, with high-pressure operation, a small footprint, and low power requirements [36-38]. Deep VUV emissions, ideal for chemical sensing, are realized by multiple pathways including resonant energy transfer between gas molecules and high energy states such as excimers [39]. Further, MHCDs generated in Si microcavities add inexpensive up-scaling of radiant output through parallel operation [7]. Figure 1-2 shows operation of a parallel array with high surface area and a 200 x 200 (40,000) cavity configuration [40]. Over the past 15 years, MDs have been explored as detectors used for photoionization [6, 30, 41], atomic emission spectroscopy [7, 9, 29, 42, 43], and mass spectroscopy [44, 45].

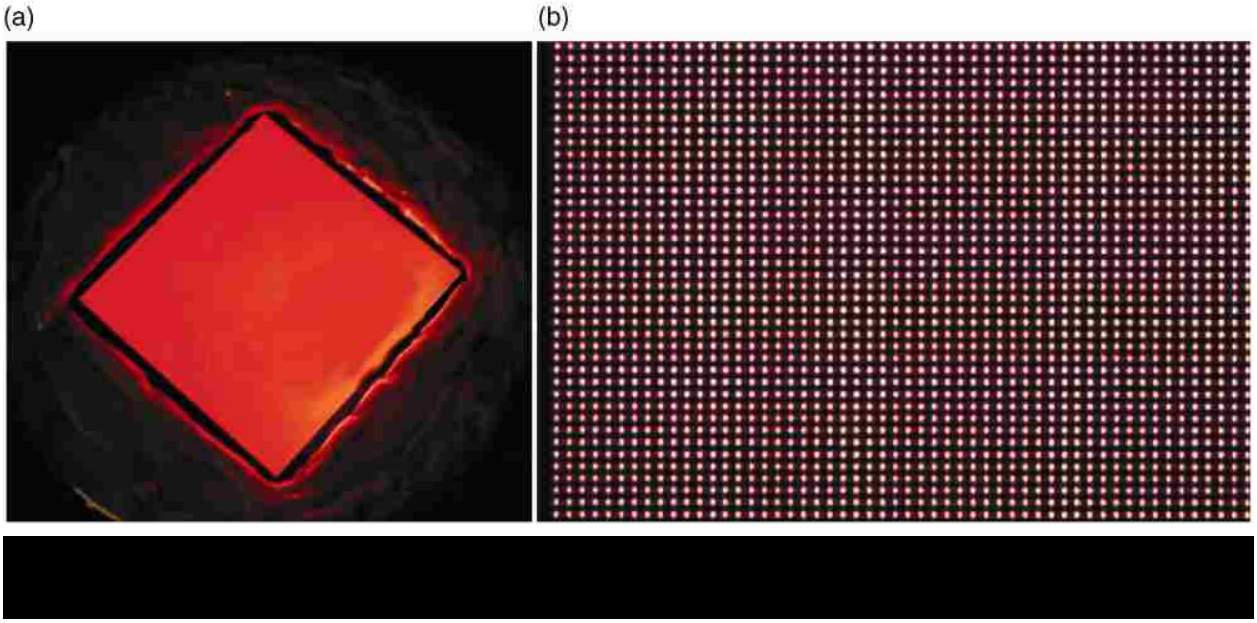

1.2.3. Contamination

An important hurdle to widespread adoption of microdischarges outside the laboratory has been an issue with contamination and the resulting spectral interference [46]. Detectors that utilize plasma as the excitation source rely on an understanding of the discharge's output

spectrum, which is a function of the make-up gas concentrations. Contamination of the plasma gas carries great importance when using a PID. The relative signal intensity from different chemical species arises from competing reactions, which are determined by the ratios of photon emissions at different wavelengths [26]. Miclea *et al* described H2O contamination as possible issue related to non-linear signal response from different analytes [9]. The group also hypothesized that Fluorine would embed in the discharge walls, further changing its expected linear response curve. Device lifetime is also degraded by glass fouling and damage to electrodes, which both increase as contaminant concentration increases [1]. Even in discharge chambers with static gas fill such as bulbs, small leaks can develop due to a mismatch in the coefficient of thermal expansion between the window materials and glass lamp housing, which both reduce the quantity of PID excitation gas and allow for contamination by outside air [1].

1.3. Plasma Fundamentals

1.3.1. Introduction to Plasma

Plasma is a state of matter consisting of ionized gas where electrons move through the medium unbound to parent atoms. When negatively charged electrons that are bound to atoms in a gas receive enough energy, they are able to escape the attraction to the positively charged protons in the atom's nucleus. This creates a state of free electrons and charged ions. Due to the charges that exist, plasma demonstrates electrically active properties such as being conductive and responding to magnetic fields. Plasmas exist on a scale from weakly ionized, where a small percentage of atoms exist as ions, to completely ionized, where all atoms exist as ions [33].

When a gas first becomes ionized, the development of plasma proceeds through a series of regimes that depend on the electrical parameters, voltage and current. As seen in Figure 1-3,

following an initial voltage application, no discharge is present and current flow is minimal (A to B). As the voltage is increased, the discharge transitions into a dark discharge where no glow is present, but some current flows (B to C to D). Once the breakdown voltage is reached, a Townsend discharge occurs and glow becomes visible (D). Immediately, the resistance drops and current increases until a normal glow is reached (D to G). Further increase in voltage leads first to an abnormal glow (G to H to I) followed by an arc (J) [33].

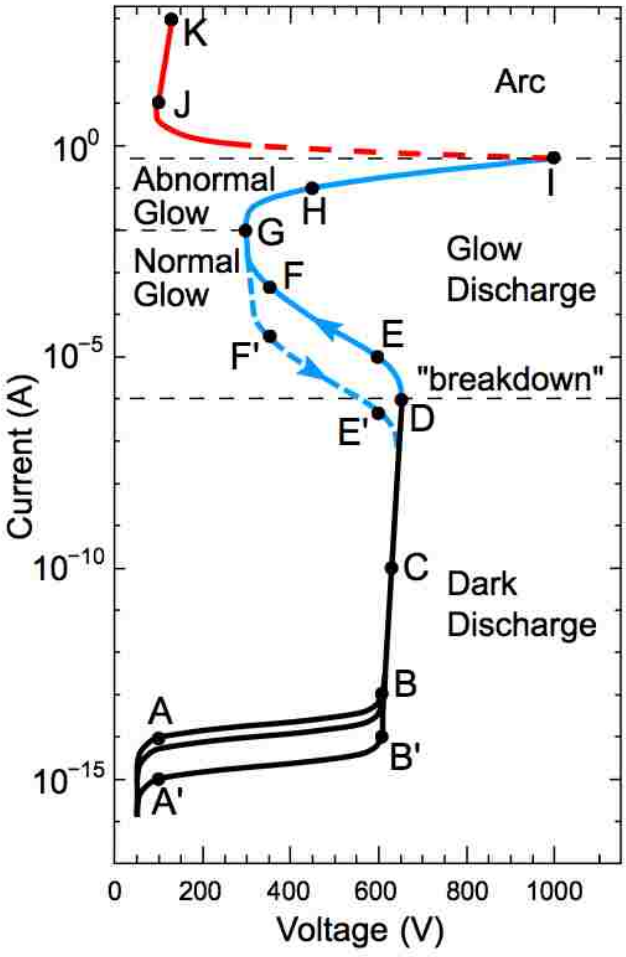

1.3.2. Thermal Equilibrium

Atmospheric pressure plasmas fall into two categories 1) local thermal equilibrium (LTE) and 2) non-local thermal equilibrium (non-LTE). In LTE plasmas, reactions and electron transitions result from collisions with electrons, neutrals, and ions, not by radiative processes [3]. This state is further defined by the microscopic reversibility of interactions such as excitation/de-excitation, ionization/recombination, kinetic energy exchange, and absorption/emission [47]. As a result, electron and heavy particle temperatures in a LTE plasma are equal [48]. Non-LTE plasmas, conversely, feature distinct temperature profiles for heavy particles (ions and neutrals – T_h) and light particles (electrons – T_e) [48]. In this case, significant radiative deexcitation of electrons in the lower energy levels causes the electron-induced excitation rate to be greater than the electron-induced deexcitation rate. This breaks equilibrium conditions, resulting in a non-Boltzmann electron energy distribution (Eq. 3). Here, conditions are governed by partial local Boltzmann and Saha equilibrium (Eq. 4) (pLSE and pLBE respectively) in which $T_S = T_{exc} = T_e >> T_h$ [47]. In equation 3, E_{qp} is the energy required to bring an atom at state p to state q, and T_{exc} is the atom's excitation temperature. In equation 4, $E_{ip,}$ is the ionization potential of atom in state p, n is the gas density, T_e is the electron temperature, and T_S is the Saha temperature. In practical terms, electrons move much faster then heavy particles and begin to control collisions and transition phenomena [3]. This effect can be especially pronounced in pulsed discharges due to the extreme difference in acceleration between heavy and light particles in transient electric fields [49].

$$Boltzmann: \ f(E_{qp}) \propto e^{\frac{-E_{qp}}{\kappa T_{exc}}} \tag{3}$$

$$Saha: \quad f(E_{ip}) \propto \frac{n}{2}\frac{h^3}{(2\pi m\kappa T_e)^{3/2}}\exp\left(\frac{-E_{\mathrm{ip}}}{\kappa T_S}\right) \tag{4}$$

In low-pressure plasma, heavy particles are excited primarily through inelastic collisions with electrons. These collisions lack the frequency to heat the neutrals and ions. As the collision rate increases, T_e drops and T_h rises until they equalize and the plasma approaches LTE. High-pressure conditions reduce the mean free paths for each particle, increasing collision frequency, which both heats the heavy particles and induces plasma chemistry.

This high-pressure regime is prone to instabilities. As heavy particles are accelerated, their surface impacts become non-negligible, causing damage and alterations, most frequently, to the cathode. Also, stepwise and penning ionization involving metastable species can cause an avalanche of secondary electron generation like a laser [50]. Further, high-pressure operation requires a high applied electric field, which can be satisfied by using a higher driving voltage or reducing the electrode gap distance. In the case of increased voltage, a third instability arises from the resulting increase in current density, particularly in the cathode sheath.

1.3.3. Paschen's Law

Paschen's Law (Eq. 5), derived in 1889 by Friedrich Pashcen, couples the breakdown voltage of a plasma to the operating pressure (p) and gap distance (d) [51].

$$V = \frac{apd}{\ln(pd)+b} \tag{5}$$

Where a and b are experimentally derived constants relating to physical parameters such as cathode material. Further simplification is possible by using the dimensionless constant

$\delta = pd/(pd)_{min}$, where $(pd)_{min}$ relates to the minimum breakdown voltage. Substitution into equation 5 yields:

$$V = V_{min}\frac{\delta}{1+\ln\delta} \tag{6}$$

The minimum breakdown voltage is then determined by tracing the curve resulting from equation 6, represented in Figure 1-4. Low-pressure operation in thus possible in the *pd* range of 1 – 10 Torr cm, where breakdown voltage is at a minimum. Under these constraints, to maintain

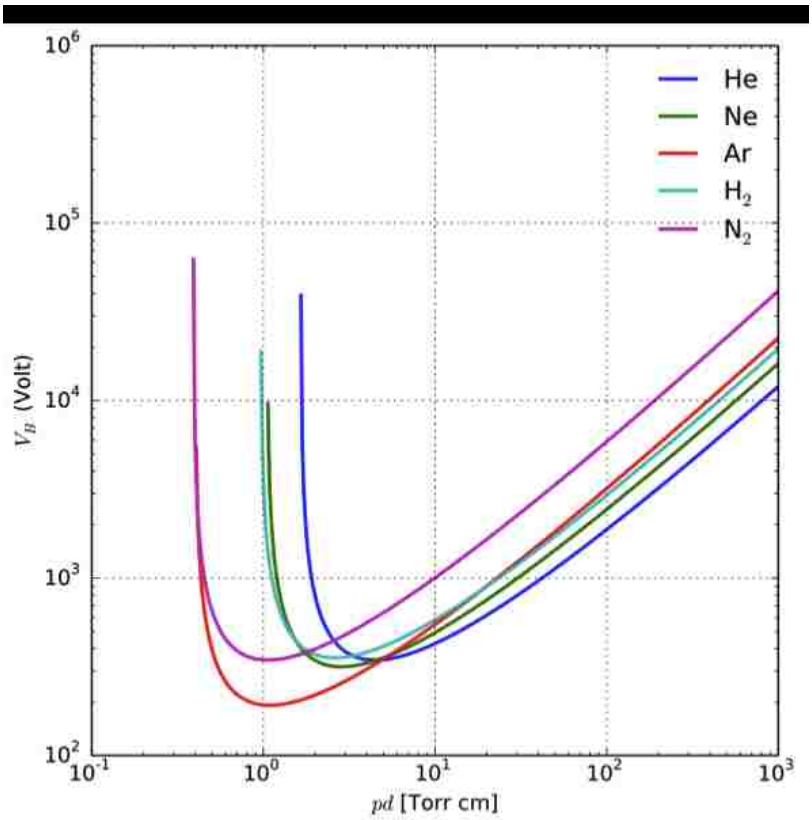

stability in high-pressure conditions, the gap distance must be decreased. Down-scaling the plasma dimensions increases its area to volume ratio (A/V). This plays a stabilizing role in microdischarges due to the predominance of boundary phenomena [3].

1.4. Microdischarges

Microdischarges are defined as weakly-ionized plasmas whose characteristic spatial dimension is between 1μm and 1mm [52, 53].

1.4.1. Radio Frequency and AC Glow Discharge

MDs have been initiated using high frequency rf signals (350 kHhz) [54, 55] as well as lower frequency AC signals (10 kHz) [40]. Hoffmann *et al* demonstrated the ignition of a 200 x 200 AC-driven silicon micro-cavity array in Ne at 500-900 torr [54].

1.4.2. Direct Current Discharge

Micro-scale DC glow discharges have been studied extensively [53, 56-61]. However, DC discharges suffer from poor device stability, consistency, and lifetime due to the sputtering effect, where high velocity ions collide with and damage the metallic electrodes [62, 63].

1.4.3. Pulsed DC Discharge

To reduce sputtering, DC MDs have been run in pulsed mode including μs pulsed mode [64, 65] and ns pulsed mode [49, 66, 67]. An increase in device life of greater than 6:1 was reported in a ns-pulsed plasma driven at 10 kHz [62]. Pulsed modes also favor higher energy transient states thought to arise from a build up of displacement current prior to breakdown voltage [62].

1.4.4. Dielectric Barrier Discharge

Dielectric barrier discharges (DBD) are generated using high voltage (1-100 kV) and high frequency (up to MHz) potential [30]. The dielectric barrier is formed by placing a dielectric material such as ceramic, glass, or a polymer against the electrode surface facing the discharge chamber [63]. DBDs feature stabile discharge homogeneity and long electrode operation lifetime [63, 68].

1.4.5. Micro hollow cathode discharge (MHCD)

In 1996, Schoenbach *et al* built the first micro hollow cathode discharge (MHCD) [69, 70], which can be operated in DC, pulsed DC, or rf. The micro hollow cathode device, shown in Figure 1-5 is a sandwich construction composed, in its simplest form, of metal-dielectric-metal layers with a hole drilled either partially or completely. The holes, typically on the order of 100-250 μm, allow for atmospheric pressure operation based on the *pd* law discussed in section 1.4.3.

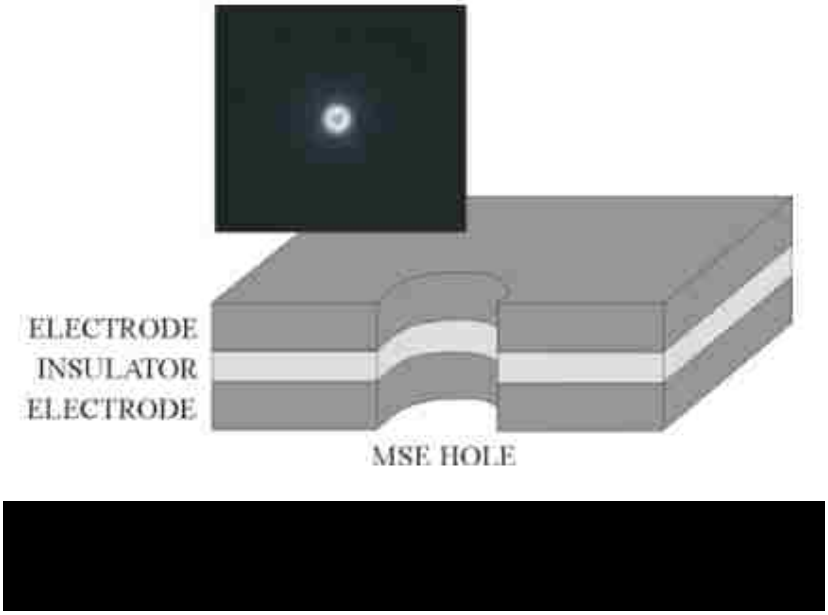

In this configuration, the *pd* scaling law is represented in accordance with microdischarge work by White [71] to be a function of *pD*, where *D* is the hole diameter.

1.4.5.1. MHCD in Silicon

As a means of simply and efficiently up-scaling the radiative power of microdischarges, arrays have been realized in silicon [8, 53, 56, 59]. Figure 1-6 shows the basic construction of a silicon microcavity. Using complementary metal oxide semiconductor (CMOS) and micro electro-mechanical systems (MEMS) technologies, microdischarge devices have been fabricated in arrays of 500 x 500 (250,000) with parallel operation [7, 40]. For specific details on device fabrication, see (Chen, Park, *et al.* 2002) [59].

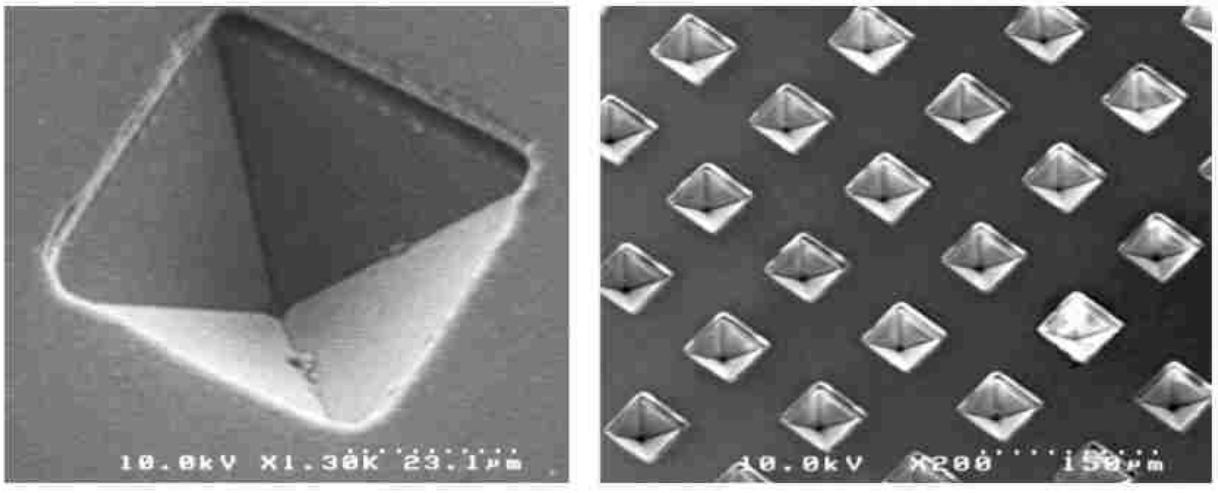

The MHCDs in silicon have been constructed in three primary geometries: the inverted-pyramid, shown in Figure 1-7 [8, 53, 59], the square vertical cavity [59], and the circular vertical cavity [56, 57, 62]. Devices have also been driven with the top electrode as the cathode [56] and in the reverse polarity [72].

1.4.5.2. Electron Temperature and Density

The electron temperature and density in a discharge is a function of the type of gas, the gas pressure, driving voltage, and electrode configuration [7]. Measuring discharge temp in a DC glow discharge in Ar showed a nearly linear growth with pressure [73]. Scaled to atmospheric pressure, the temperature and electron density of an Ar discharge is expected to be 2000 K and 10^{16} /cm^3 [73]. A MHCD in He demonstrated gas temperatures of 500 K to 800 K in the pressure range of 200 mbar to 1000 mbar respectively, nearly an order of magnitude lower than Ar under the same conditions [74]. A closed MHCD (the bore diameter and the cathode/insulator thickness had dimensions of 200μm and 100μm, respectively) was operated at 1 bar with a current of 0.5mA [75, 76]. An electron density of 1.2×10^{14} cm^{-3}, a gas temperature of 660K and an electron temperature of 10eV in the cathode sheath was reported. Electron temperature and densities for a pulsed atmospheric pressure CCD in Ne were measured with laser Thomson scattering by Bolouki *et al* [77]. They found an average n_e and T_e of 1.5 eV and 4 x 10^{22} m^{-3} respectively.

1.5. Review of Microdischarges as Detectors

To this author's knowledge, the first use of a microdischarge as a chemical detector was performed by Pedersen-Bjergaard in 1993 [55, 78]. This work used an rf microplasma generated

in a 1-mm quartz capillary in He for the detection of halogens with a reported selectivity for halogen to carbon of 10^3:1. Following works reported the detection of sulfur [55], and then H, S, Cl, Br, and I [78]. However, this arrangement used an optimum power input of 25 W, which would be difficult to consistently deploy to a field device.

The use of a MHCD in chemical sensing was first reported by Miclea *et al*. in 2002 [9]. The device construction consisted of an insulator sandwiched between two metallic foil electrodes with a hole drilled perpendicular to the layers. They showed concentration specific detection of halogenated hydrocarbons using an atmospheric pressure MHCD with He as the

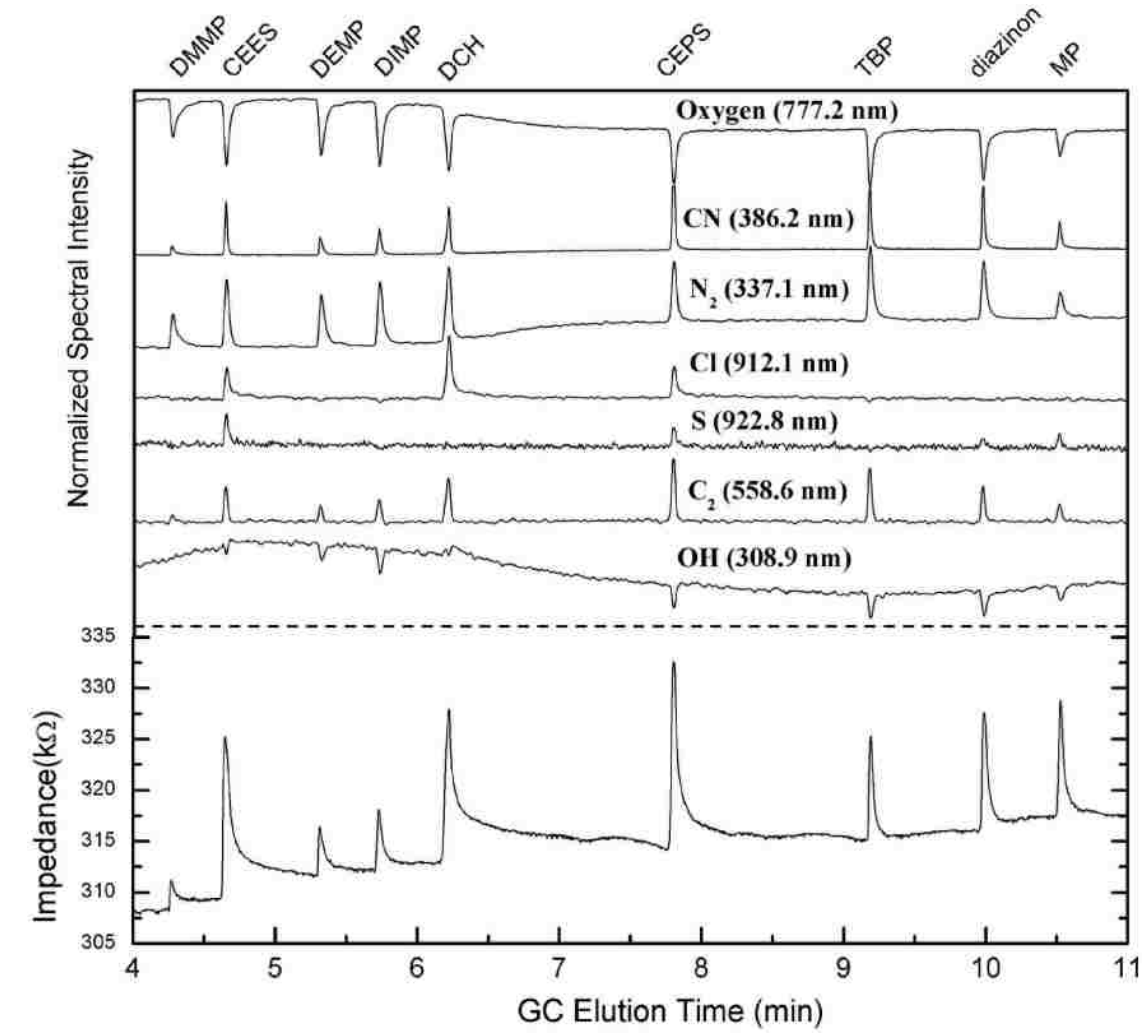

plasma gas. A lower detection limit for CCl_2F_2 of 20 ppb was reported using the emission line for Cl and F at 912.114 nm and 739.868 nm respectively. Kunze *et al* reported the detection of CH_4 and other hydrocarbons at ppm levels by recording CH emission spectra in an RF-driven microplasma [42].

In 2006, Becker *et al* reported the coupling of a DC-excited MHCD (D = 100 μm) to a 5 m gas chromatography column to detect and discriminate complex molecules [7]. Examining the unique response of a specific analyte at different wavelengths allows for a highly specific detection system. Toxic or environmentally hazardous analytes at nanogram levels were successfully and specifically detected. Figure 1-8 (top) shows the intensity of spectral emission lines during sample elution. Each trace corresponds to the relative fluorescence of specific molecular and dissociative fragments at the given wavelength. Figure 1-8 (bottom) shows the device impedance during sample elution, which provides a secondary measurement tool. In each case, the peaks correspond to the following hazardous chemical species: dimethyl methylphosphonate, 2-chloroethyl ethyl sulfide, diethyl methylphosphonate, diisopropyl methylphosphonate, dichlorohexane, 2-chloroethyl phenyl sulfide, tri-n-butyl phosphate and methyl parathion (DMMP, CEES, DEMP, DIMP, DCH, CEPS, TBP, and MP respectively).

Recently, Narayanan *et al* reported the creation of a mass-sensitive PID that used a DC microdischarge as the photoionization source [6]. Shown in Figure 1-9, the PID demonstrated the capability to detect aromatics, straight carbon chains up to octane (LOD 50 ppm), and air that was mixed with the injection. Further, the non-destructive nature of the PID allowed it to be coupled to an FID for a second analysis. Franchina *et al* compared a barrier discharge ionization detector (BID) run in He against a traditional FID for the detection of a range of analytes including saturated and aromatic hydrocarbons along with diesel fuel [41]. They found an

improved signal response of 4.1:1 over the FID, however, because the FID is mass sensitive while the BID is concentration sensitive, the FID had a lower limit of detection. In 2014, Miyahara *et al* [29] reported similar findings with a DC glow discharge in He.

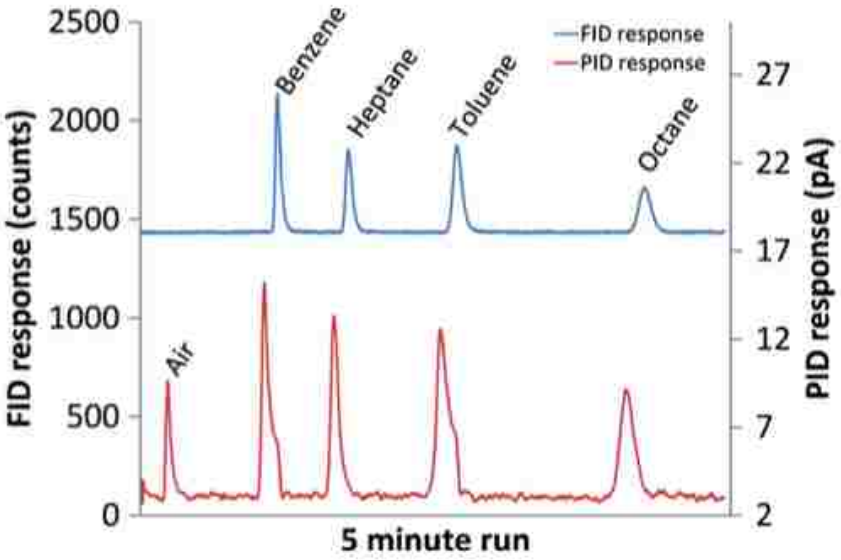

Lastly, a micro He dielectric barrier discharge photoionization detector (μHDBD-PID) was developed by Zhu *et al* [30]. Non-destructive detection of hydrocarbons, alcohols, and aromatics with high selectivity was reported. A lower detection limit on the order of pg was reported for Pentane, CCl_4, Heptane, Benzene, Toluene, Ethylbenzene, *p*-Xylene, and *n*-Nonane. While the analyte peak height showed a linear positive response with He flow rate, the signal to noise ratio reached a maximum at 20 mL/min and then declined with higher flow rates. Further, a signal to noise ratio increase of 10:1 was reported over an FID, with no change in performance over a three-week period. The discharge was run with a voltage and power of 4 kV and 385 mW respectively, which represents low power compared to bench-top devices, but is orders of magnitude higher than Si-MHCDs.

1.6. References

1. *The PID Handbook: Theory and Applications of Direct-Reading Photoionization Detectors (PIDs)*. Third ed. 2013.

2. Chetvorno. *Glow Discharge*. [cited 2017 03/25]; Available from: https://commons.wikimedia.org/w/index.php?curid=28931243

3. Kulsreshath, M.K., *Development and study of microdischarge arrays on silicon*. 2013, UNIVERSITÉ D'ORLÉANS: France.

4. Krishnavedala. [cited 2017 03/25]; CC BY-SA 4.0]. Available from: https://commons.wikimedia.org/w/index.php?curid=35233450.

5. Rocheleau, M., *Chemical Exposure Deaths on the Job Getting Rarer*, in *Boston Globe*. 2016: Boston.

6. Narayanan, S., G. Rice, and M. Agah, *A micro-discharge photoionization detector for micro-gas chromatography.* Microchimica Acta, 2013. **181**(5-6): p. 493-499.

7. Becker, K.H., K.H. Schoenbach, and J.G. Eden, *Microplasmas and applications.* Journal of Physics D: Applied Physics, 2006. **39**(3): p. R55-R70.

8. Eden, J.G. and S.J. Park, *Microcavity plasma devices and arrays: a new realm of plasma physics and photonic applications.* Plasma Physics and Controlled Fusion, 2005. **47**(12B): p. B83-B92.

9. Miclea, M., et al., *Decomposition of Halogenated Molecules in a Micro-Structured Electrode Glow Discharge at Atmospheric Pressure*, in *Hakone VIII*. 2002: Puehajaerve, Estonia. p. 206.

10. *The World Health Report 2003 - Shaping the Future*. 2003, The World Health Organization: Geneva.

11. Brinded, L., *The world faces a high likelihood of more large-scale terrorist attacks in 2017*, in *Business Insider*. 2017.

12. Fatah, D.A.A., et al., *Guide for the Selection of Chemical Detection Equipment for Emergency First Responders*. 2007, Department of Homeland Security.

13. Akbar, M., et al., *Improved performance of micro-fabricated preconcentrators using silica nanoparticles as a surface template.* J Chromatogr A, 2013. **1322**: p. 1-7.

14. Manginell, R.P., et al., *Mass-Sensitive Microfabricated Chemical Preconcentrator.* Journal of Microelectromechanical Systems, 2008. **17**(6): p. 1396-1407.

15. Shakeel, H. and M. Agah, *Self-Patterned Gold-Electroplated Multicapillary Gas Separation Columns With MPG Stationary Phases.* Journal of Microelectromechanical Systems, 2013. **22**(1): p. 62-70.

16. Rice, G. and M. Agah, *First Reconfigurable MEMS seperation columns for Micro Gas Chromatography*, in *25th iIternation Conference on Micro Electro Mechanical Systems (MEMS)*. 2012.

17. Showalter, S.K., et al., *Design and Testing of a Micro Thermal Conductivity Detector (TCD) System*. 2003, Sandia National Laboratories.

18. Rastrello, F., et al., *Thermal Conductivity Detector for Gas-Chromatography: Acquisition System and Experimental Measurements*, in *Instrumentation and Measurement Technology Conference (12MTC)*. 2012. p. 1226-1230.

19. Kuipers, W. and J. Muller, *Sensitivity of a planar micro-flame ionization detector.* Talanta, 2010. **82**(5): p. 1674-9.

20. Ho, C.K., M.T. Itamura, M. Kelley, and R.C. Hughes, *Review of Chemical Sensors for In-Situ Monitoring of Volatile Contaminants*. 2001, Sandia National Laboratories.

21. Elmi, I., et al., *A miniaturized gas-chromatographic system for the evaluation of fish freshness* in *Sensors*. 2008, IEEE. p. 1084–1087.

22. Reddy, K., et al., *On-chip Fabry–Pérot interferometric sensors for micro-gas chromatography detection.* Sensors and Actuators B: Chemical, 2011. **159**(1): p. 60-65.

23. Reddy, K., et al., *Rapid, sensitive, and multiplexed on-chip optical sensors for micro-gas chromatography.* Lab Chip, 2012. **12**(5): p. 901-5.

24. Petty, C. *Detect, Identify and Protect: Future Capabilities of Chemical Detection Methods*. 2014 [cited 2017 03/11]; Available from: http://www.cbrneportal.com/detect-identify-and-protect-future-capabilities-of-chemical-detection-methods/.

25. Liu, J., et al., *Adaptive two-dimensional microgas chromatography.* Anal Chem, 2012. **84**(9): p. 4214-20.

26. Poole, C.F., *Ionization-based detectors for gas chromatography.* J Chromatogr A, 2015. **1421**: p. 137-53.

27. Verner, P., *Photoionization detection and its applications in gas chromatography.* Journal of Chromatography, 1984. **300**(249-264).

28. Gu, X.W., L. Meng, Y. Yan, and Y.Q. Sun, *Predicted Properties of Cylindrical Microhollow Cathode Discharges in Helium Using a Two-Dimensional, Self-Consistent Fluid Model.* Contributions to Plasma Physics, 2009. **49**(1-2): p. 40-48.

29. Miyahara, H., et al., *Development and fundamental investigation of He plasma ionization detector (HPID) for gas chromatography using DC glow discharge.* Journal of Analytical Atomic Spectrometry, 2014. **29**(1): p. 105-110.

30. Zhu, H., et al., *Low-Power Miniaturized Helium Dielectric Barrier Discharge Photoionization Detectors for Highly Sensitive Vapor Detection.* Anal Chem, 2016. **88**(17): p. 8780-6.

31. Stark, R.H. and K.H. Schoenbach, *Direct current glow discharges in atmospheric air.* Applied Physics Letters, 1999. **74**(25): p. 3770.

32. Stark, R.H. and K.H. Schoenbach, *Direct current high-pressure glow discharges.* Journal of Applied Physics, 1999. **85**(4): p. 2075-80.

33. Fridman, A., *Plasma Chemistry*. 2008, NY: Cambridge University Press.

34. Kushner, M.J., *Modeling of microdischarge devices: Pyramidal structures.* Journal of Applied Physics, 2004. **95**(3): p. 846.

35. Miclea, M., M. Okruss, K. Kunze, N. Ahlman, and J. Franzke, *Microplasma-based atomic emission detectors for gas chromatography.* Anal Bioanal Chem, 2007. **388**(8): p. 1565-72.

36. Moselhy, M., R.H. Stark, K.H. Schoenbach, and U. Kogelschatz, *Resonant energy transfer from argon dimers to atomic oxygen in microhollow cathode discharges.* Applied Physics Letters, 2001. **78**(7): p. 880.

37. Shi, W., R.H. Stark, and K.H. Schoenbach, *Parallel operation of microhollow cathode discharges.* IEEE Transactions on Plasma Science 2002. **27**(1): p. 16-17.

38. Roth, M., et al. in *Proceedings of 1st International Conference On Microreactor Technology*. 1998. Springer Verlag Berlin.

39. P. Kurunczi, H.S., K. Becker, *Hydrogen Lyman-α and Lyman-β emissions from high-pressure microhollow cathode discharges in Ne H2 mixtures.* Journal of Physics B: Atomic, Molecular and Optical Physics, 1999. **32**: p. 651-58.

40. Park, S.-J., K.F. Chen, N.P. Ostrom, and J.G. Eden, *Arrays of AC-excited, silicon microdischarge devices as large as 40,000 (200 x 200) pixels: electrical and optical characteristics for operation in neon.* Electronics Letters, 2005. **41**(6): p. 311-312.

41. Franchina, F.A., et al., *Evaluation of a novel helium ionization detector within the context of (low-)flow modulation comprehensive two-dimensional gas chromatography.* J Chromatogr A, 2015. **1402**: p. 102-9.

42. Kunze, K., C.M. Herring, and J.G. Eden, Applied Physics Letters, 2006. **Submitted**.

43. Gianchandani, Y.B., S.A. Wright, C.K. Eun, C.G. Wilson, and B. Mitra, *Exploring microdischarges for portable sensing applications.* Anal Bioanal Chem, 2009. **395**(3): p. 559-75.

44. Joshua M. Symonds, A.S.G., Facundo M. Ferna´ndez, Thomas M. Orlando, *Microplasma Discharge Ionization Source for Ambient Mass Spectrometry.* Analytical Chemistry, 2010. **82**(2): p. 621-627.

45. Symonds, J.M., R.N. Gann, F.M. Fernandez, and T.M. Orlando, *Microplasma discharge vacuum ultraviolet photoionization source for atmospheric pressure ionization mass spectrometry.* J Am Soc Mass Spectrom, 2014. **25**(9): p. 1557-64.

46. Meng, F., X. Yuan, X. Li, Y. Liu, and Y. Duan, *Microplasma-Based Detectors for Gas Chromatography: Current Status and Future Trends.* Applied Spectroscopy Reviews, 2014. **49**(7): p. 533-549.

47. Moisana, M., M.D. Calzada, A. Gamero, and A. Sola, *Experimental investigation and characterization of the departure from local thermodynamic equilibrium along a surface-wave-sustained discharge at atmospheric pressure.* Journal of Applied Physics, 1996. **80**(1): p. 46-55.

48. Boulos, M.I., P. Fauchais, and E. Pfender, *Thermal Plasmas: Fundamental and applications I*. 1994, New York: Plenum Press.

49. Stephens, J., A. Fierro, J. Dickens, and A. Neuber, *Temporally resolved electron density of a repetitive, nanosecond pulsed microdischarge.* Journal of Physics D: Applied Physics, 2014. **47**(46): p. 465205.

50. Allmen, P.V., et al., *Linear, segmented microdischarge array with an active length of similar to 1 cm: cw and pulsed operation in the rare gases and evidence of gain on the 460.30 nm transition of Xe+.* Applied Physics Letters, 2003. **82**(25): p. 4447-4449.

51. Paschen, F., *Ueber die zum Funkenübergang in Luft, Wasserstoff und Kohlensäure bei verschiedenen Drucken erforderliche Potentialdifferenz.* Annalen der Physik, 1889. **273**(5): p. 69-96.

52. Park, S.-J., et al., *Microdischarge Arrays: a New Family of Photonic Devices.* IEEE J. Sel. Topics Quantum Electron., 2002. **8**: p. 387-94.

53. Eden, J.G., et al., *Microplasma devices fabricated in silicon, ceramic, and metal/polymer structures: arrays, emitters and photodetectors.* Journal of Physics D: Applied Physics, 2003. **36**(23): p. 2869-2877.

54. Hoffmann, V., et al., *Measurement of voltage and current in continuous and pulsed rf and dc glow discharges.* Journal of Physics: Conference Series, 2008. **133**: p. 012017.

55. Pedersen-Bjergaard, S. and T. Greibrokk, *On-column atomic emission detection in capillary gas chromatography using a radio frequency plasma.* Microcolumn Seperations, 1994. **6**(1): p. 11-18.

56. J. W. Frame, D.J.W., T. A. DeTemple, J. G. Eden, *Microdischarge Devices Fabricated in Silicon.* Applied Physics Letters, 1997. **71**(9): p. 1165-67.

57. J. W. Frame, P.C.J., T. A. DeTemple, J. G. Eden, *Continuous-Wave Emission in the Ultraviolet from Diatomic Excimers in a Microdischarge.* Applied Physics Letters, 1998. **72**(21): p. 2634-36.

58. Becker, K.H., P.F. Kurunczi, and K.H. Schoenbach, *Collisional and radiative processes in high-pressure discharge plasmas.* Physics of Plasmas, 2002. **9**(5): p. 2399.

59. Chen, J., S.-J. Park, Z. Fan, J.G. Eden, and C. Liu, *Development and characterization of micromachined hollow cathode plasma display devices.* Journal of Microelectromechanical Systems 2002. **11**(5): p. 536-43.

60. Schoenbach, K.H. and T.T. R. Verhappen, F. E. Peterkin, *Microhollow Cathode Discharges.* Applied Physics Letters, 1996. **68**(1): p. 13-15.

61. Kulsreshath, M.K., et al., *Study of dc micro-discharge arrays made in silicon using CMOS compatible technology.* Journal of Physics D: Applied Physics, 2012. **45**(28): p. 285202.

62. Sillerud, C.H., et al., *Characterization of chemical contaminants and their spectral properties from an atmospheric pressure ns-pulsed microdischarge in neon.* Physics of Plasmas, 2017. **24**(3).

63. Bogaerts, A., E. Neyts, R. Gijbels, and J. Van der Mullen, *Gas discharge plasmas and their applications.* Spectrochimica Acta Part B: Atomic Spectroscopy, 2002. **57**(4): p. 609-658.

64. Fliegel, D. and D. Günther, *Electrical Characteristics of a Millisecond Pulsed Glow Discharge.* Elsevier, Spectrochimica Acta Part B, 2008. **63**: p. 630-637.

65. Petzenhauser, I., L.D. Biborosch, U. Ernst, K. Frank, and K.H. Schoenbach, *Comparison between the ultraviolet emission from pulsed microhollow cathode discharges in xenon and argon.* Applied Physics Letters, 2003. **83**(21): p. 4297.

66. Schoenbach, K.H. and W. Zhu, *High-Pressure Microdischarges: Sources of Ultraviolet Radiation.* IEEE Journal of Quantum Electronics, 2012. **48**(6): p. 768-82.

67. Stephens, J., A. Fierro, D. Trienekens, J. Dickens, and A. Neuber, *Optimizing drive parameters of a nanosecond, repetitively pulsed microdischarge high power 121.6 nm source.* Plasma Sources Science and Technology, 2015. **24**(1): p. 015013.

68. Golubovskii, Y.B., V.A. Maiorov, J. Behnke, and J.F. Behnke, *On the stability of a homogeneous barrier discharge in nitrogen relative to radial perturbations.* Journal of Physics D: Applied Physics, 2003. **36**(8): p. 975.

69. Schoenbach, K.H., R. Verhappen, T. Tessnow, F.E. Peterkin, and W.W. Byszewski, *Microhollow Cathode Discharges.* Applied Physics Letters, 1996. **68**(1): p. 13.

70. Schoenbach, K.H., A. El-Habachi, W. Shi, and M. Ciocca, *High-Pressure Hollow Cathode Discharges.* Plasma Sources Science and Technology, 1997(6): p. 468-477.

71. White, A.D., *New Hollow Cathode Glow Discharge.* Journal of Applied Physics, 1959. **30**(5): p. 711.

72. Dufour, T., et al., *Effect of limiting the cathode surface on direct current microhollow cathode discharge in helium.* Applied Physics Letters, 2008. **93**(7): p. 071508.

73. Penache, C., et al., *Characterization of a high-pressure microdischarge using diode laser atomic absorption spectroscopy.* 2002. **11**(4): p. 476-483.

74. Miclea, M., K. Kunze, U. Heitmann, S. Florek, and J. Franzke, *Diagnostics and application of the microhollow cathode discharge as an analytical plasma.* Journal of Physics D: Applied Physics, 2005. **38**(11): p. 1709-15.

75. Kothnur, P. and L. Raja. in *56th Gaseous Electronics Conference*. 2003. San Franscisco, CA, USA.

76. Kothnur, P. and L. Raja, Journal of Applied Physics, 2005. **97**.

77. Bolouki, N., K. Tomita, S. Hassaballa, Y. Yamagata, and K. Uchino, *Temporal evolution of electron density and electron temperature profiles in a non-thermal atmospheric-pressure plasma measured by laser Thomson scattering.* Japanese Journal of Applied Physics, 2015. **54**(1): p. 016101.

78. Pedersen-Bjergaard, S. and T. Greibrokk, *On-Column Bromine- and Chlorine-Selective Detection for Capillary Gas Chromatography Using a Radio Frequency Plasma* Analytical Chemistry, 1993. **65**(15): p. 1998-2002.

Chapter 2

Electrical Character of a DC Microdischarge in Silicon

2.1 Microdischarge Device

Figure 2-1 shows the scale of the device compared to a US quarter. The Si discharge chip was secured to the board using conductive epoxy. The device was then wire-bonded to electrodes on the board. Finally, non-conductive epoxy was applied to the rim of the chip to avoid arcing between the device electrodes. The inset shows the four discharge cavities and the top electrode.

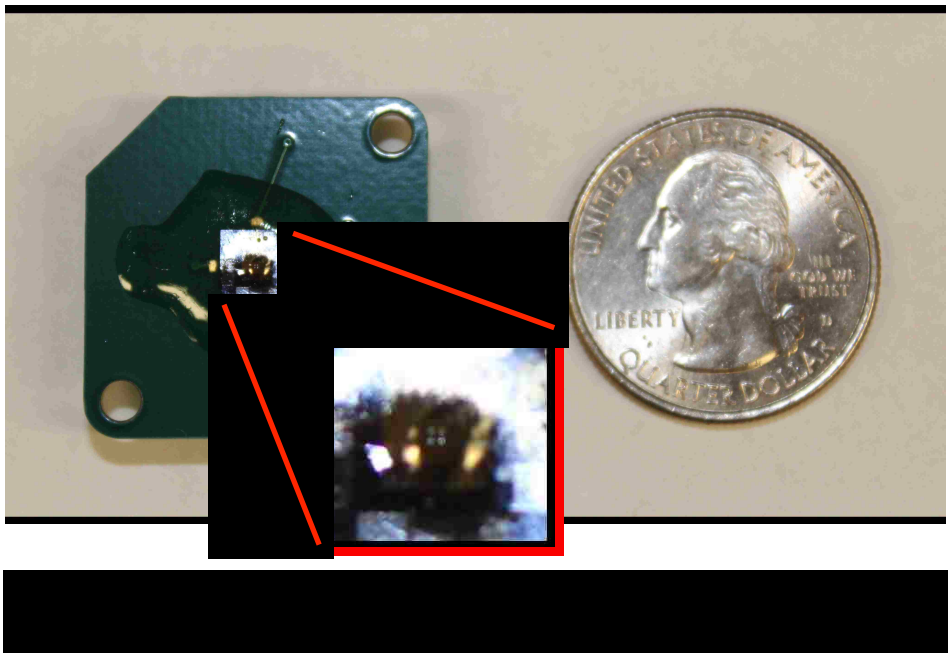

2.2 Current and Voltage Curves in DC

Figure 2-2 shows the *V-I* (voltage-current) characteristics for a four-hole array with 100 μm cavity diameter and a 100-150 μm cavity depth operated in 655 torr Ne. The discharge was driven with the top electrode as the anode. The voltage was ramped step-wise from +100 V to +800 V in increments of 50 V, with each step held for 4 s. As seen in Figure 2-2, the current stayed near zero until the breakdown voltage of + 250 V was reached, at which point the plasma ignited and a flow of current was measured. As seen

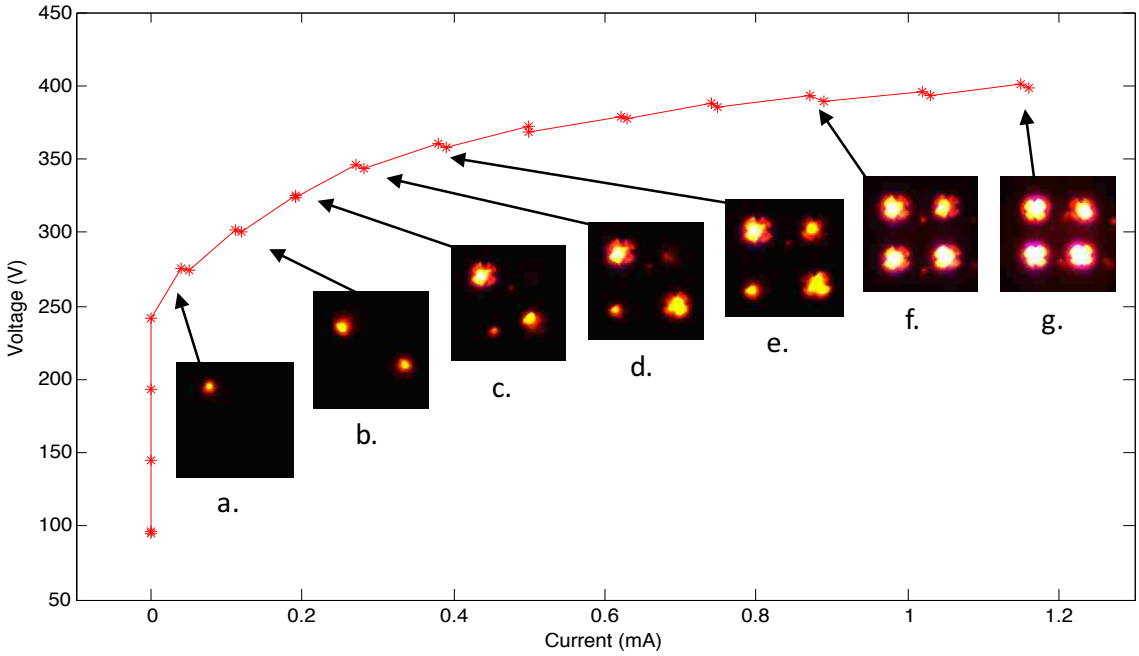

in the pictorial insets in Figure 2-2 (a-e) plasma was initiated in a hole-by-hole fashion. As the driving voltage was increased, the voltage drop across the device and the current flowing through the device also increased until the remaining three holes had ignited.

Once all four holes ignited, the curve flattened, denoting normal-glow like conditions. In this regime an increase in current corresponds to the plasma spreading over the cathode surface. A discharge of this type is sustained by harvesting surface electrons due to the increasing volume of the plasma, which keeps electron density of the discharge relatively constant [1, 2]. Under these conditions the discharge retains a relatively constant resistivity. As seen in Figure 2-2 (d-g) the increase in driving voltage led the plasma to spread along the cathode surface within the cavity until it filled the cavity entrance. This experiment was limited to +800 V driving voltage in order to preserve the device for further testing. Had a higher driving voltage been applied, it is assumed that the plasma would have extended to cover the entire inner cathode surface, at which point a further increase in driving voltage would require the harvesting of electrons from beneath the surface of the cathode. This would correspond to a sharp increase in voltage drop and the transition from a normal glow to an abnormal glow, as seen by Dufour *et al* [3]. From the images it can be concluded that the discharge current was not uniform throughout each cavity or between each cavity, probably due to micro-scale variations in material composition and shape resulting from the manufacturing process.

2.3 References

1. Fiala, A., L.C. Pitchford, and E.E. Kunhardt. *Two-dimensional, hybrid model of glow discharge in hollow cathode geometries* in *International conference on phenomena in ionized gasas*. 1995. Stevens Institue of Technology; Hoboken, NJ (United States).

2. Schoenbach, K.H., R. Verhappen, T. Tessnow, F.E. Peterkin, and W.W. Byszewski, *Microhollow Cathode Discharges.* Applied Physics Letters, 1996. **68**(1): p. 13.

3. Dufour, T., et al., *Effect of limiting the cathode surface on direct current microhollow cathode discharge in helium.* Applied Physics Letters, 2008. **93**(7): p. 071508.

Chapter 3

Examination of Contaminants Commonly Experienced by Plasma Devices Operating Outside the Laboratory

Published in the Journal, Physics of Plasmas

C. H. Sillerud et al., Physics of Plasmas **24**, 033502 (2017); doi: 10.1063/1.4977448

Characterization of Chemical Contaminants and the Spectral Properties from an Atmospheric Pressure ns-Pulsed Microdischarge in Neon

Colin H. Sillerud [1,2]; Peter D. D. Schwindt [3]; Mathew Moorman [2]; B. T. Yee [4]; John Anderson [2]; Nathaniel B. Pfeifer [2]; E. L. Hedberg [1]; Ronald P. Manginell [2]

[1] Department of Chemical and Biological Engineering, University of New Mexico, Albuquerque, NM

[2] Nano and Micro Sensors Department, Sandia National Laboratories, Albuquerque, NM

[3] Physics Based Microsystem Department, Sandia National Laboratories, Albuquerque, NM

[4] Applied Optical Plasma Science Department, Sandia National Laboratories, Albuquerque, NM

3.1 Introduction

Non-equilibrium plasmas have seen wide use, both in theoretical explorations of plasma physics and in applications such as environmental remediation of gaseous wastes [1], destruction of volatile organic compounds [2], and the detection of trace contaminants [3]. These latter uses can require time consuming sample collection in the field and transport to a lab for analysis. Microhollow cathode discharges (MHCD) generated in silicon chips offer the capabilities of non-thermal excitation sources along with an extended range of portability, atmospheric pressure operation and inexpensive silicon manufacturing. To achieve this, MHCDs utilize high energy vacuum ultraviolet (VUV) emissions that are generated via resonant energy transfer between rare gas excimers and trace gases at atmospheric pressures [4-6]. As rare-gas excimers represent highly energetic states, often on the order of 10-20 eV, contaminants present at concentrations lower than 0.01 percent can significantly impact the spectral output of a device.

If MHCDs are to gain wide use in field applications, an understanding of the impact of likely contaminants on the spectral emissions of MHCDs is necessary. Presented here is an examination of the emissions produced by the common contaminants, H_2O, O_2, H_2, and N_2, in a ns-pulsed atmospheric pressure neon microdischarge. To further explore the underlying physics responsible for experimental phenomena, a zero-dimensional (0-D) model has also been developed, which attempts to mimic the experimental conditions presented here.

MHCDs consist of an arbitrarily shaped metallic anode and a cylindrical hollow cathode open on at least one side. MHCDs typically operate in either normal glow mode, where voltage is steady as current increases, or abnormal glow mode, where voltage increases with current [7]. Under normal glow conditions, as the driving voltage is increased, the plasma spreads out over the anode to harvest an increasing number of electrons. Once the plasma reaches the limits of

the anode surface, new electrons must be harvested from within the anode bulk, which leads to an increase in voltage drop across the plasma.

As a three-body process, excimer generation requires a high collision frequency between particles of sufficient energy to facilitate the reaction. These constraints require high gas density, on the order of atmospheric pressure, and high particle energies, 16 eV or greater in the case of Ne. Hollow cathode discharges feature a non-Maxwellian energy distribution with highly energetic pendulum electrons [8] and beam electrons contributing a significant fraction to the total [9], which makes them a reasonable choice to facilitate excimer formation.

The range of operating pressures available to a MHCD device varies inversely with the hollow cathode diameter according to the Allis-White similarity law [10]. This limits the device dimensions under high pressure conditions on the order of pD = 0.1-10 Torr cm depending on gas and electrode material. In 1996 Schoenbach *et al* demonstrated the initiation of a microhollow cathode discharge with a diameter of 75 μm in pressures up to 350 Torr. Further work has since been reported plasma generation at atmospheric pressures in silicon microcavities with diameters on the order of 100 μm [11-14].

Previous work has reported driving MHCD devices in DC [14, 15], pulsed [16] and RF [17] conditions. Where DC operation allows the plasma to reach a state of steady optical emissions and current flow, pulsed and RF modes favor transient states that allow for much higher energy electrons due to pulsed electron heating [18].

3.2 Description of Array (Fabrication and Failure)

The 4-cavity microdischarge array used in these experiments was constructed in 685 µm thick p-type silicon (2-20 Ω cm). To create an insulating layer between a top electrode and the doped silicon, thermal steam oxidation was used to grow a 3 µm silicon dioxide, which was followed by the growth of a 7 µm PECVD (plasma enhanced chemical vapor deposition) silicon oxide layer. The oxide was then patterned by optical photolithography and etched a using Plasmatherm inductively coupled plasma (ICP) etcher. To form the top electrode a 200 Å

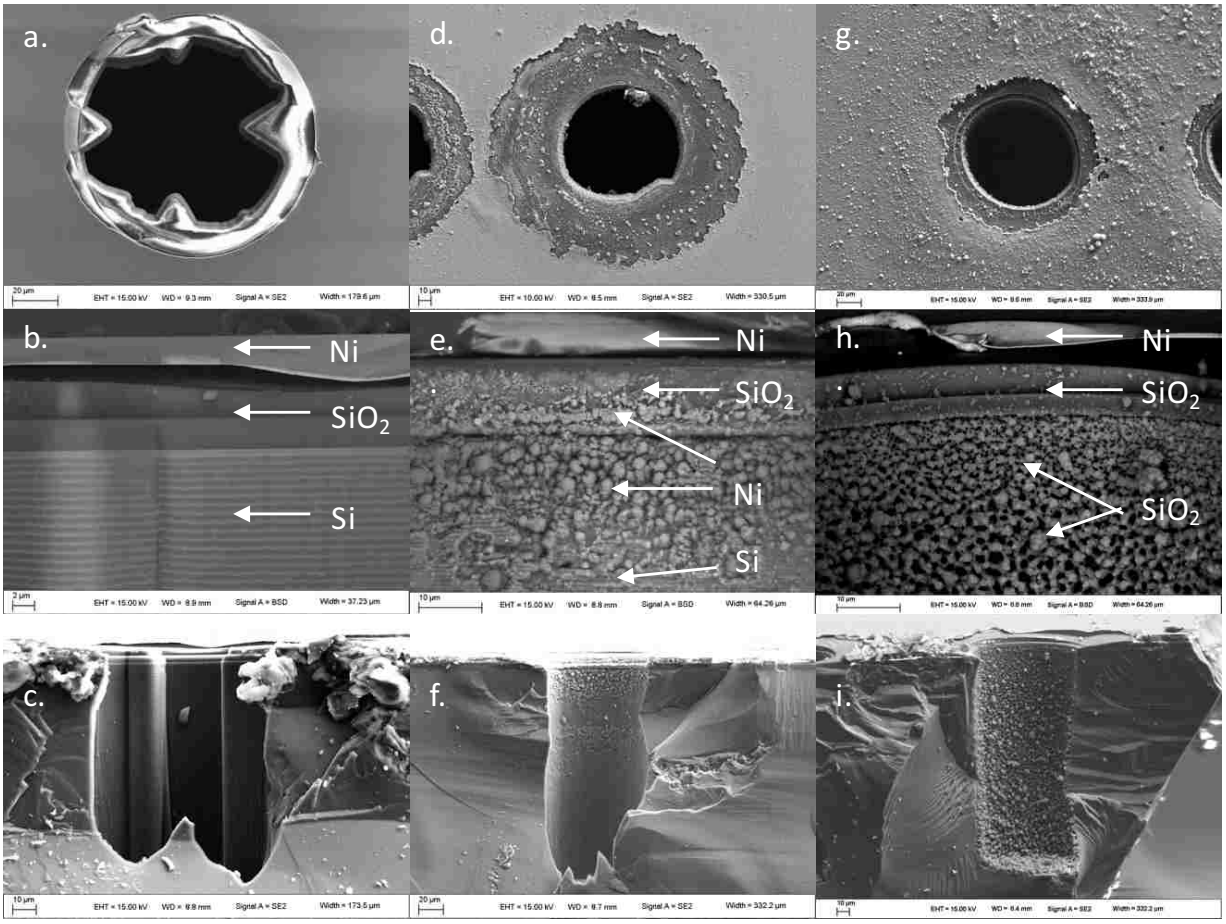

titanium adhesion layer followed by a 1 μm Nickel layer were applied via evaporation. The total surface area of the top electrode was 4 mm^2. Four cavities arranged in a 200 μm center-to-center square, 100 μm in diameter and 200 μm deep, were formed by a BOSCH deep reactive-ion etching (DRIE) process. The thermal silicon dioxide on the rear surface was then stripped using a buffered oxide etch (BOE) while the top surface was protected with photoresist. Next, an aluminum electrode was evaporated onto the rear wafer surface, which to served as an electrical ground electrode. The silicon chips were then affixed to a custom ceramic circuit board using a conductive epoxy and the top electrode was wire-bonded to an electrode pad on the circuit board. Finally, to avoid arcing, non-conductive epoxy was applied to the edges of the silicon chip and degassed for 1-2 hours in a vacuum oven set to 50 °C and evacuated to ~10 Torr. F

Figure 3-1 shows images from a scanning electron microscope (SEM) of a device before (Figure 2-1(a-c)) and after use in DC (Figure 3-1(d-f)) and ns pulsed (Figure 3-1(g-i)) modes. As can be seen in figure 3-1(a-b), prior to use, both the top electrode and the cavity surface are smooth and well defined. Analysis with energy dispersive spectroscopy (EDS) confirms the chemical make-up of the device as, from top to bottom, nickel, silicon oxide, and silicon. DC operation of microdischarge devices has been extensively covered [15, 19-21] so this paper will only discuss differences in device lifespan and failure mode between ns-pulsed and DC modes. In Figures 3-1(d-f) the device was used in DC mode until it would pass current in the absence of plasma (shorting), which is defined here as device failure. Note the extensive regression of the top nickel electrode, which is now > 40 μm from the cavity. Also notice the sputtering of nickel over the top surface and into the hole. In this case, EDS confirms the presence of nickel extending from the top layer, across the oxide and down into the silicon dielectric, which may lead to a short circuit between the electrodes as observed by Kulsreshath *et al* [21]. However,

the specific short circuit path from the electrode into the cavity could not be determined from these images. Attempts are being made to build a top electrode that is more resistant to sputtering in order to extend device life.

Pulsed operation showed multiple advantages over a DC discharge. By substantially reducing the time that the plasma was present and that current was flowing, damage to the device due to thermalization of the device walls and electrodes was avoided. Figure 3-1(h) shows that the top electrode only receded ~10 μm, much less than in DC. EDS confirms the absence of even trace amounts of nickel in either the cavity or crossing the top oxide layer. This further supports the idea that by operating in pulsed mode, thermalization of the metal electrode is reduced. On the other hand, a high concentration of oxygen is present throughout the pulsed discharge cavity. Further, when operated in ns-pulsed mode, the devices would not catastrophically fail as in DC. Current would drop and multiple ignition spikes would form over the course of a single pulse. This behavior could be reduced by increasing the driving voltage. A possible explanation is that during ns-pulsed mode oxygen reacted with the doped silicon, creating a porous insulating silicon dioxide structure on the surface of the cavity (fig. 3-1(h)). As will be discussed later, it is likely that this increased amount of oxygen in the pulsed discharge cavity caused an increase in the oxygen content within the plasma gas mixture, and a similar increase in emission of the 130.2 nm oxygen line. However, it is important to note that the species represented by the spectrums from 40-300 ns were constant over each trial, over the lifetime of each device, and did not include emissions from Si, Ni, or Ti. This suggests that the formation of spectral lines resulting from increased contamination due to sputtering of the device electrode or cavity is not a concern under these operating conditions.

Devices operated in DC mode exhibited a lifespan of 5-10 minutes of consistent use at 500 V and 655 torr Ne. On the other hand, utilizing ns-pulsed mode lead to an operational life of 45-60 min driven at ~630 V at the same pressure. Further, the integrated emission intensity from the DC discharge dropped nearly linearly by ~ 50-60 percent during operation until failure, while the ns-pulsed discharge demonstrated an initial drop of ~20 percent during break-in followed by near-stable output until behavior associated with the build up of the oxide layer discussed earlier appeared after 30-40 min.

3.3 Experimental Setup

Figure 3-2 shows the schematic of the device, circuitry, and surrounding equipment. Experiments were conducted in a ~ 1 L vacuum chamber capable of sustaining pressures in a range of 10^{-6} to 10^{3} Torr. Following evacuation with a turbomolecular vacuum pump and after the chamber was sealed off from the vacuum, the chamber pressure would immediately rise from ~10^{-5} to ~ 10^{-3} Torr, presumably due to off-gassing of the epoxy, other plastics in the chamber, and the steel chamber itself. It is assumed that this was the main contributor to gas impurities seen in the following experiments, and representative of impurities that will be seen by microdischarges in practical use. The chamber was then back-filled with the desired gas. The pressure was measured by a Pfeiffer CMR-361 pressure gauge (0.1 Torr – 825 Torr) and a Varian FRG-700 vacuum gauge (4×10^{-9} Torr – 1 Torr). To reduce the concentration of contaminants in future work, the chamber could be baked to reduce water in the steel walls, and any wiring present could be insulated using ceramic scales rather than typical plastic coatings.

Two view ports were installed on the chamber to view the plasma. The first, made of Kodial glass, faced up for direct viewing. The second, made of MgF_2, faced into a McPherson 225 one-meter vacuum spectrometer that was equipped with a 600 line/mm grating capable of 0.3 Å resolution. The spectrometer cavity was maintained at 10^{-6} Torr with another

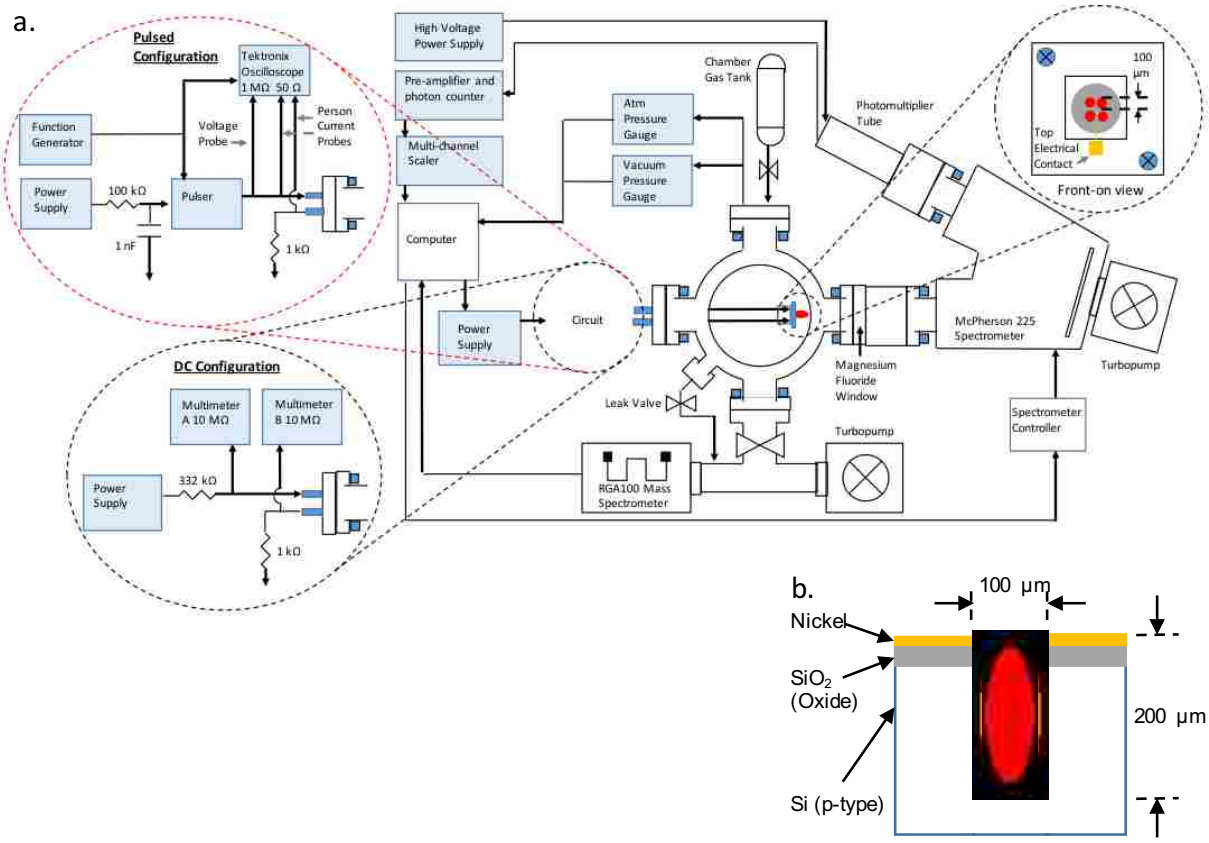

[redacted]

turbomolecular vacuum pump. The detection end of the spectrometer had a window coated with a sodium salicylate scintillating layer. Next, a Hamamatsu R6095 photomultiplier tube powered at 800 V was used to detect optical emissions. The PMT signal was amplified with a Stanford Research SR445A and acquired with a Stanford Research SR430 scaler.

A DC power supply (2500V/25W) was used to ignite the micro-discharges. Relative concentrations of chemical species in the chamber were determined with a SRS RGA 100 that

was connected to the chamber vacuum line. A leak valve was used to bleed gas into the differentially pumped vacuum line for analysis.

In pulsed mode, the circuit was reconfigured to allow the plasma to turn on quickly. A 100 kΩ resistor followed by a 1 nF capacitor were placed between the power supply and a DVI PVX-4150 pulse generator to control the load on the power supply. An Agilent 33210A function generator was used to produce a square wave pulse that initiated the pulse generator. The current was measured before and after the device using inductive current probes. A 5kV voltage probe was connected directly to the bare wire before the first current probe. A 1 kΩ resistance was placed between the last current probe and ground to serve as a ballast resistor. The voltage and current were both recorded using a Tektronix MSO 5104B oscilloscope terminated at 1 MΩ and 50 Ω respectively. The device was pulsed at a rate of 10 kHz with pulse widths between 40 – 300 ns and a duty cycle between 0.04 – 0.3 %.

This work focuses on pulsed operation with limited reference to DC operation. For reference, Figure 3-2 describes both circuits. In both the DC and the pulsed experiments the device was oriented with the top metal as the anode (biased positive) and the silicon cavity as the cathode at ground.

3.4 Model

A zero-dimensional model was created to investigate the possible processes occurring in the MHCD system [22-27] (see Section 4.3 for a complete list of reactions and references). A global model is a zero-dimensional model of a plasma which assumes spatial homogeneity. While it cannot capture the full complexity of a real plasma, it is suitable for basic

characterization of the plasma chemistry dynamics. A detailed explanation of the model follows in Section 4.1.

Briefly, most global models involve two governing equations, one for the number densities of the atomic and molecular species, and another to follow the evolution of the electron energy in the system. The former can be generally expressed as:

$$\frac{dn}{dt} = G - L \tag{1}$$

where n represents the density for some species of interest, G is the rate at which the species is produced, and L is the rate at which the species is lost. Gain and loss mechanisms vary greatly depending on the system in question and may represent excitation, ionization, detachment, or spontaneous emission among many other processes. The gain or loss terms may also represent physical processes that are not related to particle-particle interactions. One such example is the outflux of particles from the system. Despite the assumption of a zero-dimensional system, the microdischarge has boundaries which result in the outflux of particles from the region of concern. We describe this with a simple model based on the Bohm flux [28] at a surface, taking the positive ion flux to be equal to $0.61 n_i A c_s$, where n_i is the ion density, A is the characteristic collection area, and c_s is the Bohm velocity for the ion in question. The collection area is assumed to be the internal area of the microdischarge geometry. Additionally, we ignore complications in the Bohm criterion related to the presence of multiple ion species [29]. Finally, we assume that the outflux of electrons is equal to the total outflux of ions.

The dynamics of the electron energy are considered using the equation,

$$\frac{dT_e}{dt} = \frac{2}{3k_B n_e}\left[\frac{e^2 n_e E(t)}{m_e K_m n_g} - 3n_e K_m n_g \frac{m_e}{m_g}\frac{3}{2}k_b\left(T_e - T_g\right) - \sum \Delta\epsilon\right] \quad (2)$$

Here, T_e is the electron temperature, k_B is Boltzmann's constant, n_e is the electron density, E is the (time-dependent) applied electric field, K_m is the (temperature-dependent) momentum transfer rate, n_g is the neutral gas density, T_g is the gas temperature, and $\Delta\varepsilon$ is the energy change as the result of some reaction. The three terms in this equation represent the electron energy gained by the field, the energy loss due to neutral collisions, and the energy gained (or lost) due to reactions involving electrons.

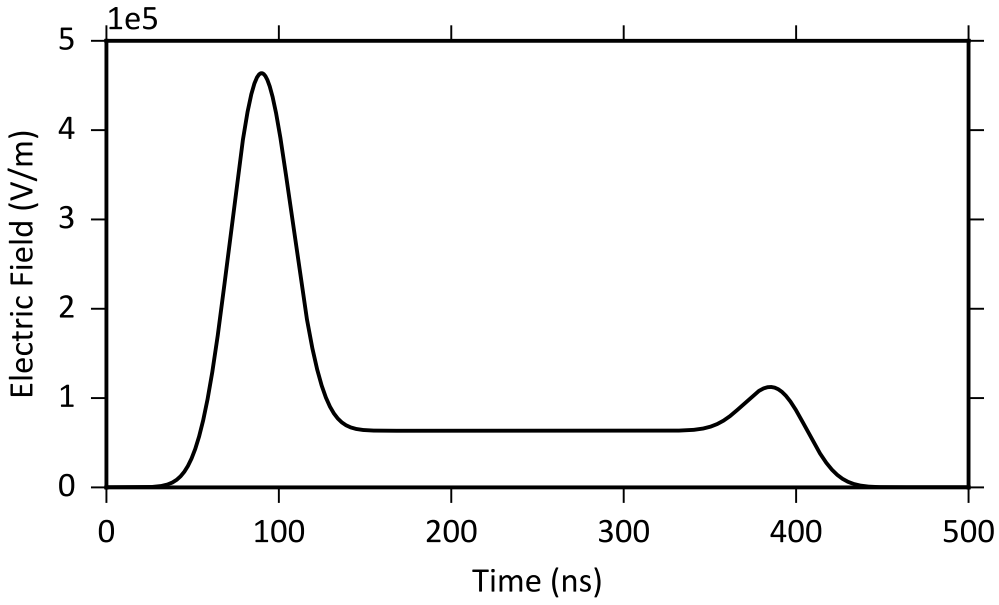

The applied electric field shape (fig. 3-3) was chosen to be consistent with the observed emission dynamics as described in section 3.5.3.

The electron energy distribution was assumed to be Maxwellian. It is probable that this assumption is not accurate during the initiation of the microdischarge given the large reduced electric fields. This will most likely result in an underestimate of the excitation rates for higher

levels. Future simulations could address this by including a bimodal electron energy distribution as described by Badareu and Popsescu [30].

3.5 Results

3.5.1 Electrical Characteristics

Figure 3-4 shows the current, voltage and optical traces during ns pulsed operation. The device current, shown in Figure 3-4(a-b), was measured and calculated using a subtractive method where the baseline displacement current due to capacitance within the system was measured by applying the standard pulsed driving voltage to the device while the device chamber was evacuated to ~ 10^{-5} Torr, a procedure which precluded the formation of a plasma. The dark current under these conditions was calculated to be on the order of one μA, which was 5 orders of magnitude below the nominal operating current. The system current was then measured during discharge operation. The baseline current was then subtracted from the active system current to give the device current.

Figure 3-4(a) compares the device optical signal measured at 585.3 nm with the device voltage and current, all during a 300 ns pulse. By comparing the discharge current to the system current in Figure 3-4(b), one can see the non-trivial displacement current present during the initiation and extinction of the pulse. While the system displacement current peaked during the initiation and extinction phases of the pulse, the actual device current reached its maximum during the standard phase between ignition and extinction. Gamez *et al*. [31] found that the electron temperature was highest during the ignition (pre-optical peak) of a neon plasma. They also found that the converse was true for electron density, which was low during pre-ignition and then increased over the course of the pulse. This corresponds with a higher optical output during

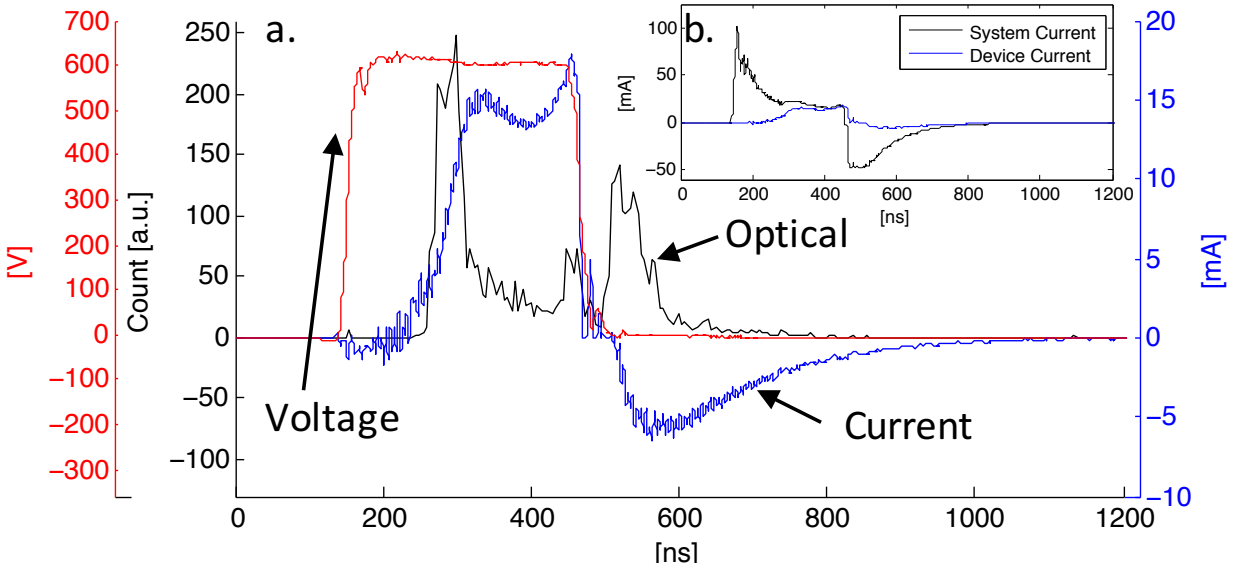

the transient stages, but a higher current in the middle stages as seen in Figure 3-4(a). The rise of the voltage pulse in Figure 3-4(a) corresponds with the displacement current spike in black in Figure 3-4(b), which both occur 100 ns prior to the ignition of the discharge. This 100 ns delay is not well understood, but may be due to the formation of a predischarge state in the plasma prior to full ignition of the normal discharge.

Figure 3-5 shows visible emissions during operation in pulsed mode at pulse widths of 40, 160, and 300 ns, all pulsed at 10 kHz. Note the near uniform character of the plasma with respect to single cavities as well as the uniformity when comparing cavities to each other. The operating conditions during these experiments were within the bounds of an abnormal discharge (6.55 Torr cm) with an increase in the highly energetic tail of the electron energy distribution [12], which allows for increased creation of high energy states such as the neon excimer.

Under conditions where the voltage rise time (t_V) is much faster than the characteristic time for kinetic energy transfer between electrons and the neutral gas atoms (τ_e), electrons reach higher energies in the transient stages of the plasma than during standard operation [32]. In our

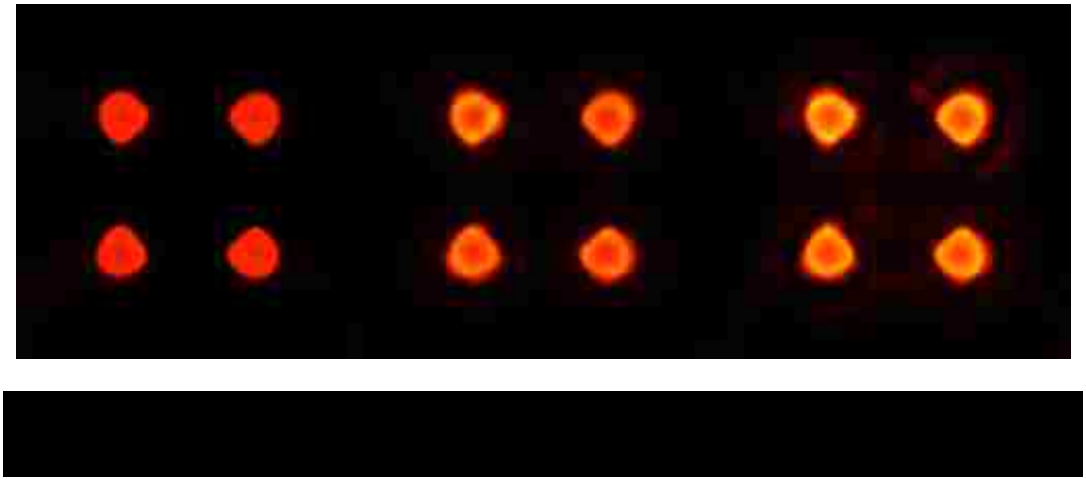

case, the measured voltage rise time (10-90% of peak voltage) was 21.5 ns. Bolouki *et al* [33] used Thompson electron scattering under conditions similar to those presented in this paper to determine an electron temperature of ~ 2.5 eV at 15 ns after initiation of the plasma, which leads to a $\tau_e = 10^6$ ns [32]. Our system is thought to have an electron temperature closer to 4.5 eV ($\tau_e = 10^4$ ns) based on simulation, which will be discussed later. During discharge initiation, space charge is negligible and electrons in the system are exposed to the full electric field. Electron densities are small, but their mean energy is likely higher (or comparable to) the reaction energy thresholds that will be discussed later. After initiation, space charge becomes important and likely pushes most of the potential drop to a small sheath region. Thus, a large portion of the plasma becomes relatively field free, resulting in a drop in electron temperature.

3.5.2 Chamber gas

A differentially pumped SRS RGA100 was used to determine relative concentrations of gas species based on their partial pressures. The highest concentration contaminants present in the discharge chamber were N_2 (0.17%), H_2 (0.14%), H_2O (0.04%), and O_2 (0.04%), with neon comprising the balance. The reported values were acquired by first subtracting the baseline from the chamber RGA signal, then correcting for the RGA's relative sensitivity using the

manufacturer's published values. These measured values were constant over the course of each experiment. However, as the RGA was sampled from the vacuum line rather than the discharge chamber, further analysis with the RGA closer to the sample is required to determine if the concentrations showed measureable variation over a single pulse width.

3.5.3 Optical Traces

Presented here are the results from the MHCD device in pulsed mode. The device was pulsed in the range of 40-300 ns at 10 kHz with a power supply biased to +950 V. Due to the internal resistance of the pulser, the voltage applied to the device was approximately +630 V as measured from the voltage probe. The chamber was backfilled to 655 Torr with Ne. To eliminate arcing between the device wires and the vacuum chamber, fish-spine ceramic insulators were installed on the wires between the chamber electrical feedthroughs and the device. As the RGA results showed, the plasma gas primarily contained the species Ne, H, O, N and N_2.

For the following analysis, representative lines were chosen for each species to examine the temporal character of their emissions. The 120.0, 121.6, 130.2, 337.1 and 585.3 nm lines correspond to N (I), H (I), O (I), N_2 (I) and Ne (I) respectively.

Figure 3-6 shows the optical traces from the individual emission lines over different pulse widths normalized by dividing by each species maximum value. Each trace is the average of three scans conducted in a random order. In each panel, the 585.3 nm Ne line is plotted in grey to give a frame of reference for each species. This line results from the transition from the $2s^2 2p^3 (^4S^o) 3s\ ^3S^o$ 1 state down to $2s^2 2p^4\ ^3P$ 1 state [23].

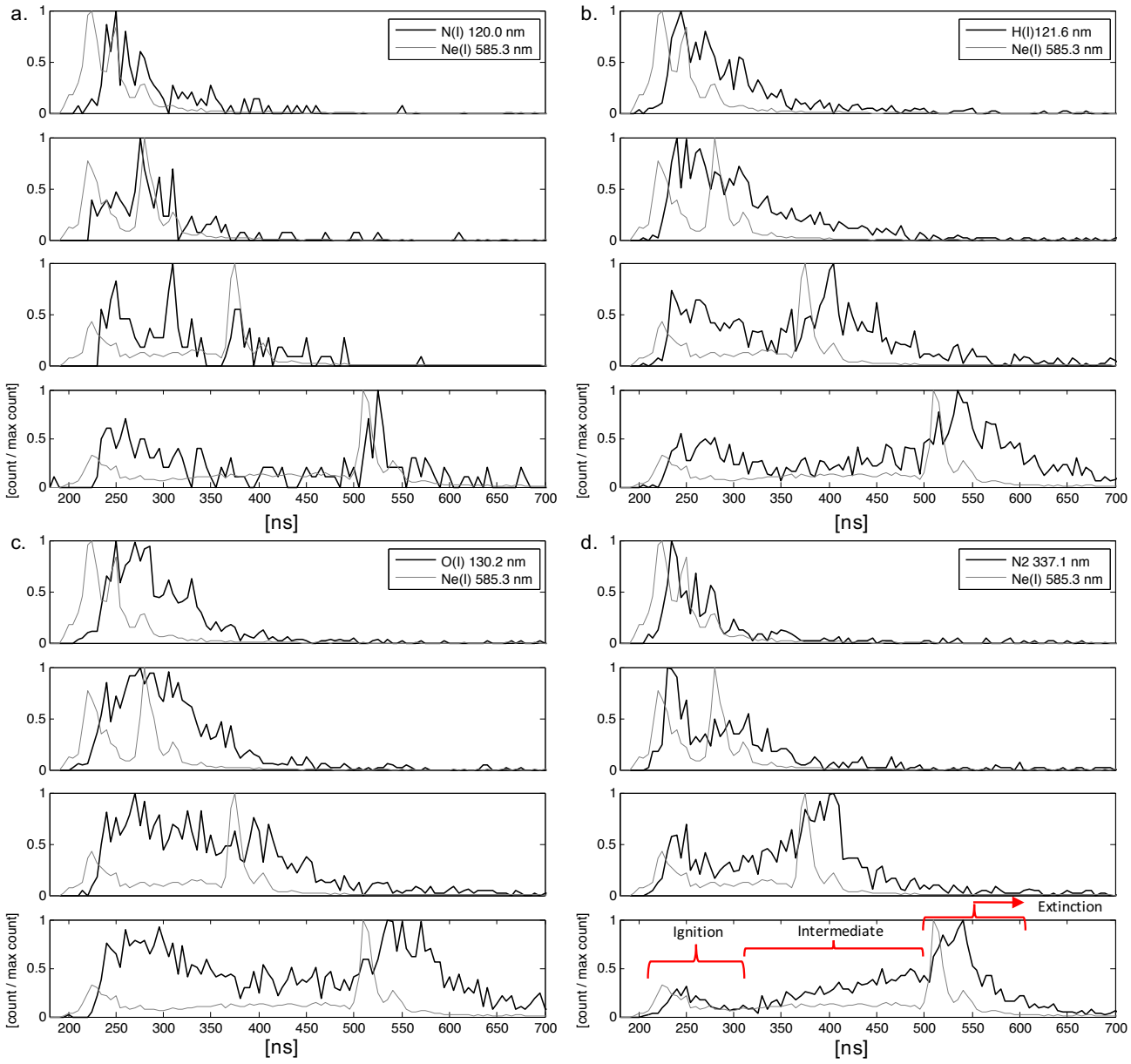

The emission pulse can be broken into three parts, which were exhibited by each species investigated here. Briefly, as shown in Figure 3-6(d), the emissions are observed to peak soon after the pulse is applied, which we term, ignition. This is followed by a decline in emission termed the intermediate stage. As the pulse ends and the applied voltage goes to zero, we witness a second ignition spike corresponding with a spike in displacement current, which we

call, extinction. The ignition peak is believed to be caused by high fields in the bulk of the device prior to the formation of significant space charge. As the plasma density increases to the point where it can shield out the applied field, much of the potential drop is removed to the boundary of the plasma, thus reducing the field experienced by the bulk of the plasma. In the 40 ns pulse regime the ignition and extinction phases were compressed together and the intermediate phase was not observed.

In each pulse length, the ignition and extinction peaks from the Ne line preceded that of the contaminant species by 20-40 ns, as seen in figure 2-6(a,b,c). The Ne emission then dropped dramatically as the other species ignited and finally settled at a semi-stable output as seen in the intermediate portion of pulses > 90 ns. A possible explanation is that emissions from H (I), O (I), and N (I) are all ground state transitions and are thus subject to radiation trapping, where a photon from a ground state transition is reabsorbed by another ground state atom of the same type as the donor. The second atom then emits a photon of the same wavelength. This process continues until a photon escapes the area with atoms of the same type as the donor, in our case, the ~ 200 μm deep plasma. This effect serves to delay the emission signal and extend the effective lifetime of the emitting state. As shown by Sumida and Fan [34], radiation trapping can be present even in optically thin plasmas.

In this study, the 337 nm line was focused on to investigate emissions from the second positive band of N_2 (figure 3-6(d)). Following the emission of the Ne line, molecular nitrogen was the next to emit. The primary N_2 (I) line at 337.1 nm followed Ne's first peak by 12 ± 5 ns. During the intermediate phase, where the Ne line showed a flat output, the N_2 (I) line showed a period of sustained linear growth in intensity. It is likely that, following the initial transition responsible for the 337.1 nm line ($C^3\Pi_u \rightarrow B^3\Pi_g$), the nitrogen molecule achieved a metastable

state [35] by degrading through the first positive system $B^3\Pi_g \rightarrow A^3\Sigma_u^+$ [36]. As the metastable state, $A^3\Sigma_u^+$ is at 5.169 eV [37], the nitrogen electron in this arrangement requires only 5.86 eV to be promoted back to $C^3\Pi_u$ (Figure 3-7), substantially lowering the energy barrier for emission of the 337.1 nm line. Also, both pathways $A^3\Sigma_u^+ \rightarrow C^3\Pi_u$ and $X^1\Sigma_g^+ \rightarrow C^3\Pi_u$ can be accomplished in a single step, while the excitation of H and O requires dissociation and excitation, which can be accomplished in one step, but only at energies > ~ 15 eV.

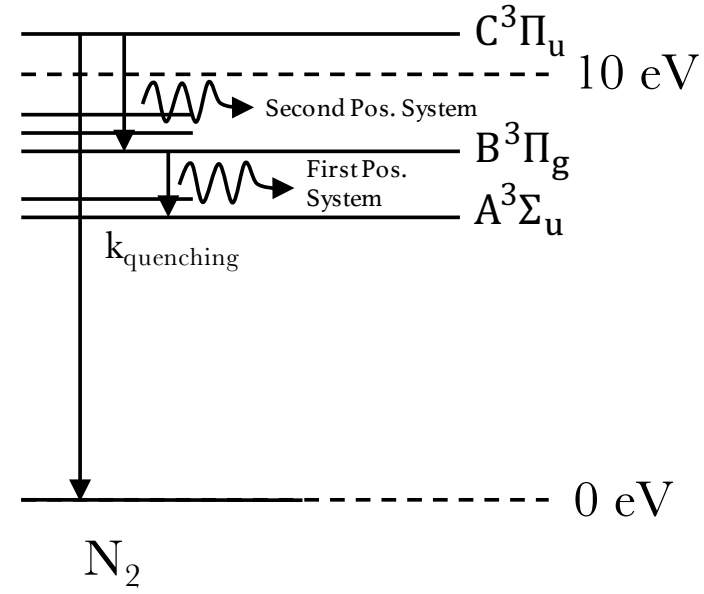

The study of atomic oxygen was carried out by focusing on the 130.2 nm line of O (I) (Figure 3-6(c)), which is part of a tight triplet created by the energy level transition from $2s^2 2p^3(^4S^o)3s\ ^3S^o\ 1$ down to $2s^2 2p^4\ ^3P\ 1$ [23]. While the other species exhibited an ignition 'spike' lasting 25-50 ns, the O (I) line displayed an ignition 'plateau' that persisted on the order of 100 ns with a slower rate of decay than the other species during the intermediate stage, again suggesting that non-trivial emission trapping could be present, likely due to an increased oxygen concentration within the plasma. This behavior is also exhibited after the extinction spike.

The Lyman-α line of Hydrogen at 121.6 nm (Figure 3-6(b)) mirrors the behavior of the Ne line, but with a similar delay to that of N (I). It peaked following Ne by 17 ±4 ns. Like the N_2 (I) line, the H (I) line also exhibited a positive slope over the intermediate period during the 300 ns pulse, suggesting that an excitation source of sufficient energy, either electrons or Ne excimers, were still present in the intermediate stage.

The excited N (I) line at 120.0 nm, resulting from the transition between $2s^2 2p^2(^3P)3s\ ^4P$ 1/2 down to $2s^2 2p^3\ ^4S^o$ 3/2 [23], was the last to show peak emission, reaching its first maximum 20 ± 9 ns after the first maximum of the Ne (I) line. Emission from N (I) first requires the disassociation of N_2 with a much higher dissociation energy (9.75 eV) than H_2 or O_2. Further, while the total dissociation and excitation energy required for the N (I) line is roughly the same as the excitation energy for the Ne line, excitation for Ne is a single step process and Ne is present at a much greater concentration. Further, while excitation of the Ne 120.0 nm line requires roughly the same energy as the Ne line at 585.3 nm (~20 eV), the concentration of Ne is > 3 orders of magnitude greater than N.

3.5.4 Integrated Emissions

Figure 3-8 shows the line-specific optical output as a function of pulse width integrated over each pulse from both the experiment (Figure 3-8(a)) and the model (Figure 3-8(b & c)). The data have been normalized by subtracting the lowest value of each species then dividing by the maximum value of the 585.3 nm line in order to focus on the relative behavior of each species. The values reported in Figure 3-8(a) were corrected via a calibration transfer function. The transfer function was created by obtaining a spectrum from a 632 McPherson deuterium lamp with our spectrometer system, which was then divided by calibrated spectra provided by

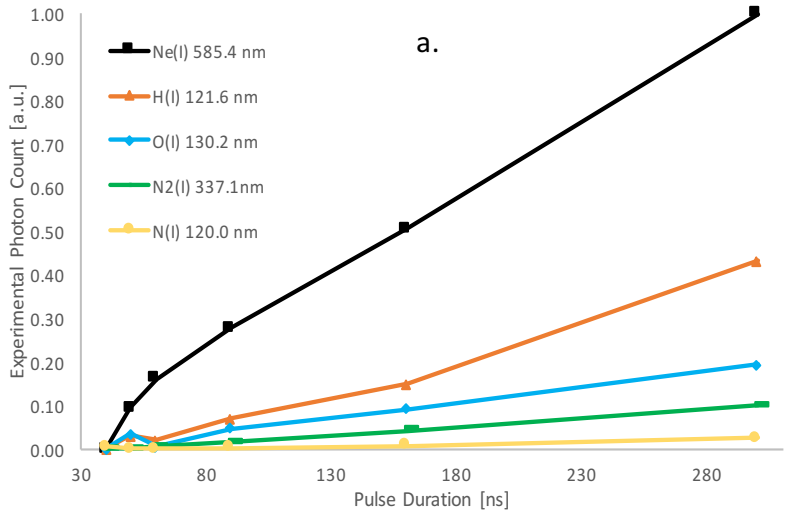

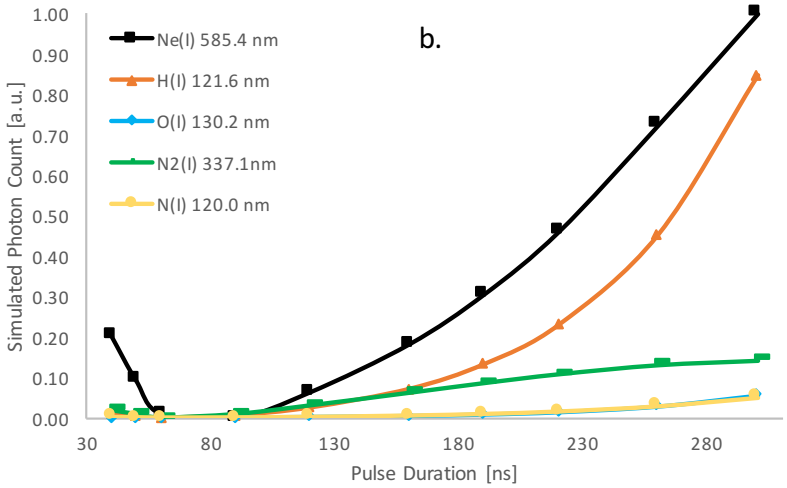

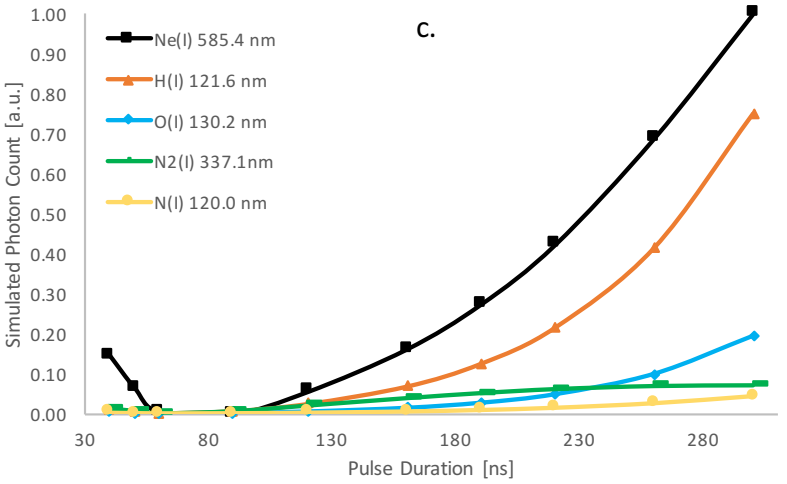

[redacted]

McPherson. Though the specific lamp used here was not calibrated, the provided spectra were found to vary over the sample space by < 10 %. As a result, we assume our final values contain

at least that level of uncertainty. The calibrated PMT data were then divided by the energy associated with each line to yield a relative photon count, which is a comparable value, both between lines and between experiment and model.

Figure 3-8(b) shows the results from the model using the gas concentrations that were measured during the experiment. As can be seen when comparing Figure 3-8(a) and (b), the model predicts a far lower emission from the oxygen line than was witnessed experimentally. As mentioned in the section, *Description of array (fabrication and failure)*, it was determined to be likely that a higher concentration of oxygen existed in the chamber than was measured. This is likely due to oxygen reacting with the silicon in the cavity. To produce figure 2-8(c), the oxygen concentration was increased ~ 300 % to equal that of hydrogen, which produced an increase in oxygen emissions, though not to the level witnessed experimentally. We present this as further evidence that the oxygen within the chamber was higher than was measured in the bulk chamber gas. Secondly, as the oxygen emissions increased, the hydrogen emissions decreased. We hypothesize that it is likely that oxygen and hydrogen share at least one similar excitation pathway.

Wieser *et al* [4] demonstrated that resonant energy transfer between neon excimers and hydrogen (eq. 3 & 4) contaminants was a possible excitation source for the Lyman-α line at 121.6 nm. Kurunczi *et al* [5] further characterized the reaction pathway by demonstrating an inverse relationship between the intensity of the Lyman-α line and the 1st and 2nd continuum of the Ne excimer band as a function of the relative concentrations of H and Ne.

$$Ne_2^* + H_2 \rightarrow 2Ne + H + H^* \quad (3)$$

$$H^* \rightarrow H + \gamma(121.6\ \text{nm}) \quad (4)$$

While the densities of the species of interest (O and H) were predicted by the model to be on the order of ~ 10^{21} – 10^{22} particles m^{-3}, the model also showed a non-trivial Ne excimer density of 10^{19} particles m^{-3}. Further, as discussed previously, it is likely that the electron energy distribution features a larger potential for high energy electrons due to a non-thermal distribution, which would increase the excimer concentration. As a result, it is reasonable to assume that excimers contribute to the plasma reaction pathways.

The transition energy released during the decay of the Ne_2^* excimer molecule is 14.8±0.8 eV, which compares favorably with the sum of the dissociation and excitation energies of H_2 (14.68 eV) [38] that are responsible for the Lyman-α line. Compare this to the the dissociation and excitation energies for O_2, which sum to 14.67 eV to achieve the state 2p3(4S*)3s.3S*.1, which produces the 130.2 nm line presented in this paper. Due to the similar total energy relating to the oxygen process (eq. 5 & 6), it is possible that the same resonant process occurs and could help explain the shifted emissions seen between H (I) and O (I) in figure 2-8(b & c). Moselhy *et al* also speculated that the resonant process was present between argon and oxygen under similar conditions [6].

$$Ne_2^* + O_2 \rightarrow 2Ne + O + O^* \quad (5)$$

$$O^* \rightarrow O + \gamma(130.2\ \text{nm}) \quad (6)$$

On the other hand, the integrated emissions from the N (I) line at 120.0 nm stayed nearly constant between pulse widths of 40 to 300 ns both experimentally and in both modeled conditions. Nitrogen, with a dissociation energy of 9.75 eV, has no such direct resonant pathway for excitation of the observed state. As this feature has the highest energy barrier, it is likely that the 120.0 nm line is excited primarily during the ignition and extinction phases of the pulse when a greater concentration of high energy electrons is present. As seen in Figure 3-6, atomic nitrogen emission is detected primarily during the transient ignition and extinction spikes.

Several additional radiative transitions are tracked by the model as detailed in the reactions table (appendix A). In Figures 3-8(b) and (c) the transitions plotted are those for which experimental data were available. It should be noted that the radiative transition rates used were those for *untrapped* emissions. As discussed earlier, the VUV emissions are all resonance radiation which should be treated appropriately. However, given the complex geometry and unknown experimental densities of atomic oxygen, hydrogen, and nitrogen in the volume between the discharge and the spectrometer window no accounting was made for this effect. In reality, trapping would be expected to increase the effective lifetime of the trapped states shifting the peaks of these emissions relative to untrapped transitions such as $Ne(2p_1) \rightarrow Ne(1s_2)$.

Another notable difference between the model and experiment is that the model predicts a semi-parabolic trend with emissions peaking at 40 and 300 ns. This is most likely due to the way the modeled electric field is treated during pulses < 90 ns. In this regime, the ignition and extinction pulses (Figure 3-3) begin to overlap and are summed into one larger peak, producing a higher field during this combined ignition/extinction period. An examination of the experimental displacement current showed that this did not occur and that the ignition and extinction spikes

remained separate. Without this feature, it is thought that the model will show a positive slope across the entire sample space as currently seen between the pulse widths of 90-300 ns.

3.6 Conclusion

In future field-portable devices that utilize microdischarges, certain gas impurities will likely be a constant presence and concern. Here we examined the spectral emissions of common impurities field-portable devices would experience – N_2, O_2, and H_2 – to characterize typical features witnessed during ns pulsing. Here we present the first, to this author's knowledge, detailed study of these specific contaminant species and their optical emission characteristics as produced by a ns-pulsed MHCD array in a silicon microcavity array. Together, our experiments and model support the hypothesis that the emissions from species capable of near-resonant energy transfer with Ne excimers are more prominent during the high energy transient stages of a ns-pulsed microdischarge. On the other hand, emission from N_2 shows the highest tendency to increase during the intermediate stage of the plasma. Specifically, the emissions of the examined chemical species varied based on their excitation potentials, and the reactions that utilized resonant energy transfer with Ne excimers (O_2, H_2) (eq 1-4) were favored during ignition and extinction, while those that featured metastable states (N_2: $A^3\Sigma_u^+ \rightarrow C^3\Pi_u \rightarrow B^3\Pi_g$) were favored during the intermediate period. This led to high transient emissions from the 121.6 nm and 130.2 nm lines, while emission from N_2 at 337.1 nm featured a prolonged increase during the intermediate period. Emission at the 120 nm line of N(I), which was the state with the highest energy barrier to excitation, showed very little change in integrated intensity and primarily emitted during the ignition and extinction pulses. The ignition and extinction phases also corresponded with a spike in displacement current produced by the system circuitry.

Also presented is an analysis of the failure modes of the devices when operated in DC vs ns-pulsed mode. It was found that in DC operation, sputtered nickel from the top electrode was visible crossing the insulating oxide layer and that the device would fail by passing current without the ignition of a plasma. Failure for a ns-pulsed device may have followed the growth of an insulating oxide layer around the inside of the doped silicon cavity, which could be alleviated by increasing the applied voltage to regain normal function until the layer became to thick for any current to flow. It is likely this reaction increased the cavity oxygen concentration by a factor of four or greater, which led to substantially increased emissions of the 130.2 nm triplet than was predicted based on measured chamber gas concentrations.

A zero-dimensional model was presented as further evidence for the specific reactions that are thought to be responsible for the relative strength of each line. The comparison between model and experiment demonstrated it was likely that the chamber concentration of oxygen was a poor measure of the actual oxygen reacting in the plasma cavity. Further adjustments to the model are underway, such as the inclusion of a non-Maxwellian electron temperature distribution.

3.7 References

1. Penetrante and Schultheis, *Non-Thermal Plasma Techniques for Pollution Control*. Vol. 34. 1993: Springer-Verlag Berlin Heidelberg.

2. Koutsospyros, A., S.M. Yin, C. Christodoulatos, and K. Becker, *Destruction of hydrocarbons in non-thermal, ambient-pressure, capillary discharge plasmas.* International Journal of Mass Spectrometry, 2004. **233**(1-3): p. 305-315.

3. Becker, K.H., K.H. Schoenbach, and J.G. Eden, *Microplasmas and applications.* Journal of Physics D: Applied Physics, 2006. **39**(3): p. R55-R70.

4. Wieser, J., et al., *Lyman-alpha emission via resonant energy transfer.* Atomic Molecular Optical Physics, 1998. **31**: p. 4589-4597.

5. P. Kurunczi, H.S., K. Becker, *Hydrogen Lyman-α and Lyman-β emissions from high-pressure microhollow cathode discharges in Ne H2 mixtures.* Journal of Physics B: Atomic, Molecular and Optical Physics, 1999. **32**: p. 651-58.

6. Moselhy, M., R.H. Stark, K.H. Schoenbach, and U. Kogelschatz, *Resonant energy transfer from argon dimers to atomic oxygen in microhollow cathode discharges.* Applied Physics Letters, 2001. **78**(7): p. 880.

7. Foest, R., M. Schmidt, and K. Becker, *Microplasmas, an emerging field of low-temperature plasma science and technology.* International Journal of Mass Spectrometry, 2006. **248**(3): p. 87-102.

8. Stockhausen, G. and M. Kock, *Proof and analysis of the pendulum motion of beam electrons in a hollow cathode discharge.* Journal of Physics D: Applied Physics, 2001. **34**: p. 1683-1689.

9. Gill, P. and C.E. Webb, *Electron energy distributions in the negative glow and their relevance to hollow cathode lasers.* Journal of Physics D: Applied Physics, 1977. **10**: p. 299-311.

10. Helm, H., *Experimenteller Nachweis des Pendel-Effektes in einer zylindrischen Niederdruck-Hohlkathoden-Entladung in Argon.* Z. Naturforsch, 1972: p. 1812-1820.

11. J. W. Frame, D.J.W., T. A. DeTemple, J. G. Eden, *Microdischarge Devices Fabricated in Silicon.* Applied Physics Letters, 1997. **71**(9): p. 1165-67.

12. K. H. Schoenbach, A.E.-H., Wenhui Shi, Marco Ciocca, *High-Pressure Hollow Cathode Discharges.* Plasma Sources Science and Technology, 1997(6): p. 468-477.

13. K. H. Schoenbach, A.E.-H., Mohamed M. Moselhy, Wenhui Shi, Robert H. Stark, *Microhollow Cathode Discharge Excimer Lamps.* Physics of Plasmas, 2000. **7**(5): p. 2186-91.

14. Becker, K.H., P.F. Kurunczi, and K.H. Schoenbach, *Collisional and radiative processes in high-pressure discharge plasmas.* Physics of Plasmas, 2002. **9**(5): p. 2399.

15. Schoenbach, K.H., R. Verhappen, T. Tessnow, F.E. Peterkin, and W.W. Byszewski, *Microhollow cathode discharges.* Applied Physics Letters, 1996. **68**(1): p. 13.

16. Moselhy, M., W. Shi, R.H. Stark, and K.H. Schoenbach, *Xenon excimer emission from pulsed microhollow cathode discharges.* Applied Physics Letters, 2001. **79**(9): p. 1240.

17. Bass, A., C. Chevalier, and M.W. Blades, *A capacitively coupled microplasma (CCμP) formed in a channel in a quartz wafer.* J. Anal. At. Spectrom., 2001. **16**(9): p. 919-921.

18. Stark, R.H. and K.H. Schoenbach, *Electron heating in atmospheric pressure glow discharges.* Journal of Applied Physics, 2001. **89**(7): p. 3568.

19. Fiala, A., L.C. Pitchford, and E.E. Kunhardt. *Two-dimensional, hybrid model of glow discharge in hollow cathode geometries* in *International conference on phenomena in ionized gasas*. 1995. Stevens Institue of Technology; Hoboken, NJ (United States).

20. Dufour, T., et al., *Effect of limiting the cathode surface on direct current microhollow cathode discharge in helium.* Applied Physics Letters, 2008. **93**(7): p. 071508.

21. Kulsreshath, M.K., et al., *Study of dc micro-discharge arrays made in silicon using CMOS compatible technology.* Journal of Physics D: Applied Physics, 2012. **45**(28): p. 285202.

22. Kushner, M.J., *Modeling of microdischarge devices: Pyramidal structures.* Journal of Applied Physics, 2004. **95**(3): p. 846.

23. Kramida, A., Y. Ralchenk, J. Reader, and N.A. Team, *NIST Atomic Spectra Database* N.I.o.S.a. Technology, Editor. 2015: Gaithersburg, MD.

24. Itikawa, Y., *Cross sections for electron collisions with nitrogen molecules.* Journal of Physical Chemistry Reference Data, 2006. **35**(1): p. 31-53.

25. Itikawa, Y., *Cross sections for electron collisions with oxygen molecules.* Journal of Physical Chemistry Reference Data, 2009. **38**(1): p. 1-20.

26. Itikawa, Y. and A. Ichimura, *Cross sections for collisions of electrons and photons with atomic oxygen.* Journal of Physical Chemistry Reference Data, 1990. **37**(2): p. 637-651.

27. Yoon, J.-S., et al., *Cross sections for electron collisions with hydrogen molecules.* Journal of Physical and Chemical Reference Data, 2008. **37**(2): p. 913-931.

28. Chen, F., *Introduction to Plasma Physics and Controlled Fusion*. 2 ed. 1984, New York: Plenum Press.

29. Baalrud, S.D., J.D. Callen, and C.C. Hegna, *Instability-enhanced collisional effects and Langmuir's paradox.* Phys Rev Lett, 2009. **102**(24): p. 245005.

30. Badareu, E. and Popescu, *Researches on the Double Cathode Effect.* Journal of electronics and control, 1958. **4**(6): p. 503-514.

31. Gamez, G., A. Bogaerts, and G.M. Hieftje, *Temporal and spatially resolved laser-scattering plasma diagnostics for the characterization of a ms-pulsed glow discharge.* Journal of Analytical Atomic Spectrometry, 2006. **21**(3): p. 350.

32. Belenguer, P., M. Ganciu, P. Guillot, and T. Nelis, *Pulsed Glow Discharges for Analytical Applications.* Elsevier, 2009: p. 19.

33. Bolouki, N., K. Tomita, S. Hassaballa, Y. Yamagata, and K. Uchino, *Temporal evolution of electron density and electron temperature profiles in a non-thermal atmospheric-pressure plasma measured by laser Thomson scattering.* Japanese Journal of Applied Physics, 2015. **54**(1): p. 016101.

34. Sumida, D.S. and T.Y. Fan, *Effect of radiation trapping on fluorescence lifetime and emission cross section measurements in solid-state laser media.* Optics Letters, 1994. **19**(17): p. 1343-1345.

35. Wilkinson, P.G., *Forbidden Band Systems in Nitrogen. I. The Vegard-Kaplan System in Absorption.* The Journal of Chemical Physics, 1959. **30**(3): p. 773.

36. Flagan, R. and J. Appleton, *Excitation Mechamisms of the Nitrogen First-Positive and First-Negetive Radiation at High Temperature.* The Journal of Chemical Physics, 1971. **56**(3): p. 1163-1173.

37. Itikawa, Y., et al., *Cross Sections for Collisions of Electrons and Photons with Nitrogen Molecules.* Journal of Physical and Chemical Reference Data, 1986. **15**(3): p. 985.

38. Sharp, T.E., At. Data, 1971(2): p. 119.

Chapter 4

A Global Model for the Examination of the Impacts of Plasma Chemistry Dynamics on Emission Spectra

4.1. Introduction

Modeling was carried out in collaboration with the Applied Optical/Plasma Science team at Sandia National Laboratories. Dr. Ben T. Yee was responsible for creating, operating, and explaining the following model [1].

A global model was developed in order to better understand the chemical reaction processes that led to the recorded parameters (emissions, temporal characteristics…). Such a model is zero-dimensional with assumed spatial homogeneity. Experimentally, the spectral output of the cavity integrated over the cavity exit was recorded. This result was an average of the emissions taken over the bulk plasma, the cathode fall and anode fall regions. It did not capture the intricacies of each region within the plasma. As a result, while the model was unable to capture the full complexity of a real plasma, it provided a suitable approximation on par with the level of the instrumentation used. Further, the simplicity of the model allowed for rapid iteration on the plasma chemistry and fast solutions. This was especially advantageous in this situation due the high complexity of the gas composition.

4.2. Equations

For clarity, details of the model's construction and operation will be represented here along with a more thorough description of results. The model utilized two governing equations, one for the number densities of the atomic and molecular species, and another for the evolution of the electron energy of the system. The former is generally expressed as:

$$\frac{dn}{dt} = G - L \tag{4-1}$$

where n is the density of the species of interest, G is that species' production rate, and L is that species' loss rate. Gain and loss terms can vary widely from system to system. Examples include, but are not limited to, excitation, ionization, detachment, and spontaneous emission. A list of reactions included in the model can be found in Table 4-1. The gain/loss mechanisms relating to each process are expressed as the densities of the species of interest multiplied by a rate constant, k. The units of k vary based on the process and the number of bodies present. For example:

$$\frac{dn_j}{dt} = k_G n_j - k_L n_j \tag{4-2}$$

Where, respectively, k_G and k_L are the gain and loss rate constants relating to species j, and n_j is the that species' density.

The gain/loss terms may also represent physical processes unrelated to particle-particle integrations, such as particle outflux from the system. In the physical system, electrons, ions and neutrals are constantly ejected from the opening of the plasma cavity. They also impact both the cathode and anode, which removes them from the system. To account for this, a simple model was built based on the Bohm flux [2] at a surface. In this case, the positive ion flux is $0.61(n_i A c_s)$, where n_i is the ion density, A is the characteristic collection area, and c_s is the Bohm velocity of the ion in question. The collection area is assumed to be the surface area of the microdischarge geometry. The Bohm velocity assumes single ion species, however, this is not the case in reality. For simplicity, the Bohm criterion for multiple ion species is ignored [3].

$$\frac{dT_e}{dt} = \frac{2}{3k_B n_e}\left[\frac{e^2 n_e E(t)}{m_e K_m n_g} - 3n_e K_m n_g \frac{m_e}{m_g}\frac{3}{2}k_b\left(T_e - T_g\right) - \sum \Delta\epsilon\right] \tag{4-3}$$

Here, T_e is the electron temperature, k_B is Boltzmann's constant, n_e is the electron density, E is the (time-dependent) applied electric field, K_m is the (temperature-dependent) momentum transfer rate, n_g is the neutral gas density, T_g is the gas temperature, and $\Delta\varepsilon$ is the energy change as the result of some reaction. The three terms in this equation represent, from left to right, the electron energy gained by the field, the energy loss due to neutral collisions, and the energy gained (or lost) due to reactions involving electrons. The gas temperature (T_g) is assumed to be constant at 300 K, in accordance with the assumption of a non-LTE plasma.

The above equations provide the foundation for the global model. Provided initial conditions, a set of reactions with associated rate or cross section data, and an electric field, we may solve for the evolution of the excited states in the system.

4.3. Plasma Chemistry

The reactions implemented in the global model along with their rates or cross-section reference are provided in Table 4-1. Several commendable compilations and models were used in the assembly of the reaction data [4-9]. A total of 27 species are considered with 47 potential reactions.

Many reactions, that were thought to be of secondary importance, were left out of the model due to the small quantities of the molecular species, the short timescale, and the desire to simply establish a qualitative understanding. The list of reactions in Table 4-1 emphasize direct excitation of emitting states and other processes that are believed to be important to the observed behavior (resonant energy transfer [10], dissociative excitation, and excimer formation).

Table 4-1 Reaction rates used in the global model. Rate constants are given in units of m^3s^{-1} unless otherwise noted. When a rate constant is omitted, rates were calculated from cross section data. Neon states are given using Paschen notation. Excited states of molecular nitrogen are in the triplet manifold. Excited atomic hydrogen, oxygen, and nitrogen are those states contributing to observed VUV emissions.

	Reaction	Rate	Ref.	Comments
Atomic Neon				
1	$e^- + Ne \rightarrow Ne + e^-$	-	[11]	
2	$e^- + Ne \rightarrow Ne(1s_5) + e^-$	-	[11]	
3	$e^- + Ne \rightarrow Ne(1s_3) + e^-$	-	[11]	
4	$e^- + Ne \rightarrow Ne(2p_1) + e^-$	-	[11]	
5	$e^- + Ne \rightarrow Ne(1s_2) + e^-$	-	[11]	
6	$Ne(1s_2) \rightarrow Ne$	6.11×10^{8} s^{-1}	[5]	
7	$Ne(2p_1) \rightarrow Ne(1s_2)$	6.82×10^{7} s^{-1}	[5]	
8	$e^- + Ne \rightarrow Ne^+ + e^- + e^-$	-	[11]	
9	$e^- + e- + Ne^+ \rightarrow Ne(2p_1) + e^-$	5.0×10^{-39} $T_e^{-4.5}$	[4]	All recombination assumed to go to $Ne(2p_1)$
10	$Ne(1s_2) + Ne(1s_2) \rightarrow Ne^+ + Ne + e^-$	3.2×10^{-16}	[12]	
11	$Ne(1s_2) + Ne(1s_3) \rightarrow Ne^+ + Ne + e^-$	3.2×10^{-16}	[12]	
12	$Ne(1s_2) + Ne(1s_5) \rightarrow Ne^+ + Ne + e^-$	3.2×10^{-16}	[12]	
13	$Ne(1s_3) + Ne(1s_3) \rightarrow Ne^+ + Ne + e^-$	3.2×10^{-16}	[12]	
14	$Ne(1s_3) + Ne(1s_5) \rightarrow Ne^+ + Ne + e^-$	3.2×10^{-16}	[12]	
15	$Ne(1s_5) + Ne(1s_5) \rightarrow Ne^+ + Ne + e^-$	3.2×10^{-16}	[12]	
16	$Ne(1s_5) + Ne + Ne \rightarrow Ne_2^* + Ne$	3.05×10^{-45} m^6s^{-1}	[13]	
17	$Ne(1s_3) + Ne + Ne \rightarrow Ne_2^* + Ne$	4.98×10^{-45} m^6s^{-1}	[13]	
Molecular Neon				
18	$e^- + Ne_2^* \rightarrow Ne + Ne + e^-$	1.0×10^{-13}	[4]	
19	$e^- + Ne_2^* \rightarrow Ne_2^+ + e^- + e^-$	$9.75\times10^{-15}T_e^{0.71}\exp(-3.4/T_e)$	[14]	
20	$e^- + Ne_2^+ \rightarrow Ne(2p_1) + Ne$	$1.7\times10^{-13}T_e^{-0.43}$	[15]	All recombination assumed to go to $Ne(2p_1)$
21	$Ne_2^* \rightarrow Ne + Ne$	3.6×10^{8} s^{-1}	[16]	
22	$Ne_2^* + Ne_2^* \rightarrow Ne_2^+ + Ne + Ne + e^-$	1.0×10^{-17}	[4]	
Atomic Hydrogen				
23	$e^- + H \rightarrow H + H^*$	-	[17]	
24	$H^* \rightarrow H$	4.70×10^{8} s^{-1}	[18]	
Molecular Hydrogen				
25	$e^- + H_2 \rightarrow e- + H + H$	-	[9]	Dissociation cross section minus (27)
26	$e^- + H_2 \rightarrow e- + H^* + H$	-	[19]	Emission cross section for Lyman-α
27	$e^- + H_2 \rightarrow e^- + H_2+ + e^-$	-	[9]	Total ionization cross section
Atomic Oxygen				
28	$e^- + O \rightarrow e^- + O^*$	-	[8]	
29	$O^* \rightarrow O$	3.41×10^{8} s^{-1}	[20]	
Molecular Oxygen				
30	$e^- + O2 \rightarrow e^- + O + O$	-	[21]	Dissociation minus (32)
31	$e^- + O2 \rightarrow e^- + O^* + O$	-	[22]	Emission cross section
32	$e^- + O2 \rightarrow e^- + O^+ + e^-$	-	[6]	Total ionization cross section
Atomic Nitrogen				
33	$e^- + N \rightarrow N^* + e^-$	-	[23]	
34	$N^* \rightarrow N$	4.07×10^{8} s^{-1}	[24]	
Molecular Nitrogen				
35	$e^- + N_2 \rightarrow e^- + N + N$	-	[7]	Total dissociation cross section for

				neutral products minus (37)
36	$e^- + N_2 \rightarrow e^- + N^* + N$	-	[21]	
37	$e^- + N_2 \rightarrow e^- + N_2(A)$	-	[7]	
38	$e^- + N_2 \rightarrow e^- + N_2(B)$	-	[7]	
39	$e^- + N_2 \rightarrow e^- + N_2(C)$	-	[7]	
40	$e^- + N_2 \rightarrow e^- + N_2^+ + e^-$	-	[7]	Total ionization cross section
41	$N_2(C) \rightarrow N_2(B)$	$2.39 \times 10^7\ s^{-1}$	[25]	v=0
42	$N_2(B) \rightarrow N_2(A)$	$8.85 \times 10^4\ s^{-1}$	[26]	v=0
Mixed				
43	$Ne^+ + N_2 \rightarrow N_2^+ + Ne$	2.9×10^{-18}	[27]	
44	$Ne_2^* + H_2 \rightarrow Ne + Ne + H + H^*$	3.0×10^{-17}	[10]	
45	$Ne_2^* + O_2 \rightarrow Ne + Ne + O + O^*$	3.0×10^{-17}	[10]	Assumed the same as hydrogen
46	$Ne(1s_3) + N_2 \rightarrow N_2^+ + e^- + Ne$	8.4×10^{-17}	[28]	Assumed same as $1s_5$
47	$Ne(1s_5) + N_2 \rightarrow N_2^+ + e^- + Ne$	8.4×10^{-17}	[28]	

4.4. Results

The equations for particle densities and electron energy were solved using the SciPy [29] implementation of the Dormand and Prince Runge-Kutta method of order 8 [30]. The applied electric field shape was chosen to be consistent with the observed emission dynamics, which were observed to peak ~ 100 ns after the pulse was applied, followed by a decline to relatively constant emission, ending with a peak after the applied voltage had gone to zero (Figure 3-4). The initial peak is likely caused by the high fields in the bulk of the device prior to the formation of significant space charge and the build-up of displacement current in the system wiring. Once space charge accumulated and the breakdown voltage was reached, the plasma ignited. From this point, the plasma density increased and could shield out the applied field, removing much of the potential drop to the cathode and anode fall regions at the boundary of the plasma [4, 31], thus reducing the field experienced by the bulk of the plasma.

4.4.1. Electric Field

Figure 4-1 depicts the applied field for one of the simulations. The width of the depicted pulse is 160 ns, however all simulations featured the same field for the first peak, the

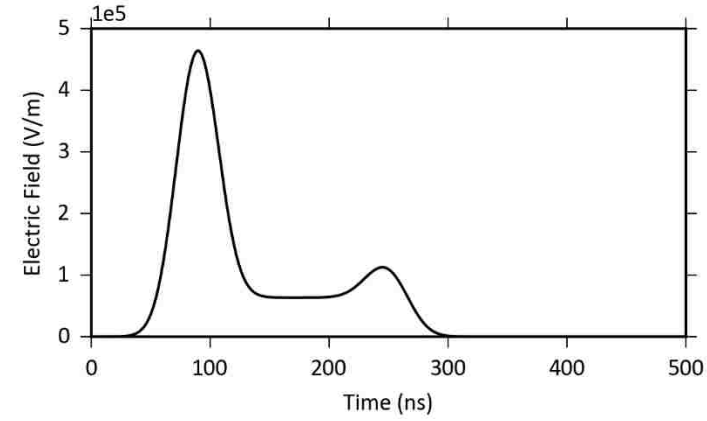

intermediate period, and the final peak: 22 Townsends (Td), 3 Td, and 5 Td respectively. The width of the pulses at the beginning and end of the discharge period are set to be 30 ns based on the observed emission behavior. In the case of the first peak, this is believed to represent the period of time necessary for space charge to become significant and the intermediate steady state to establish. The amplitude of the fields were selected on the basis that they produced similar temperatures and densities to Thomson scattering measurements of a similar discharge [32].

4.4.2. Electron Temperature

The electron energy distribution was assumed to be Maxwellian and can be seen in **Figure 4-2** for the 160ns case. It is probable that this assumption is not accurate during the initiation of the microdischarge given the large reduced electric fields. This will most likely result in an underestimate of the excitation rates for higher levels. Future simulations could be improved by the use of approximate solutions to the Boltzmann equation or Monte-Carlo methods to establish more accurate electron energy distribution functions for use in the rate calculations. Ultimately, kinetic simulations of the actual geometry, such as those carried out by Dufour [33], will be required to understand the potential impact of non-local electron kinetics.

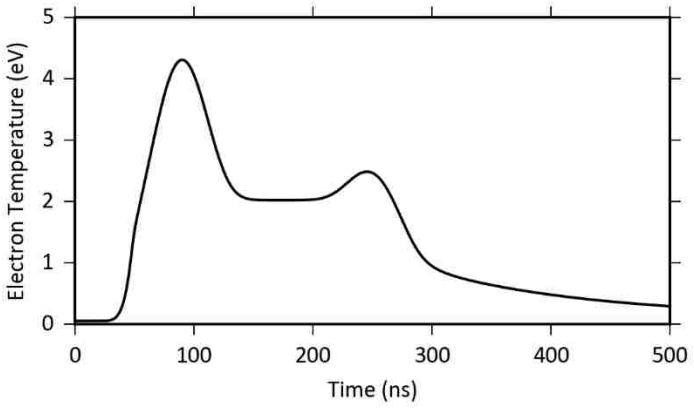

[redacted]

4.4.3. Excited States of Neon

Figure 4-3 depicts the dynamics of the excited neon states. For reference, a density of 10^{12} is approximately equal to a single particle in the volume of the microdischarge device. The

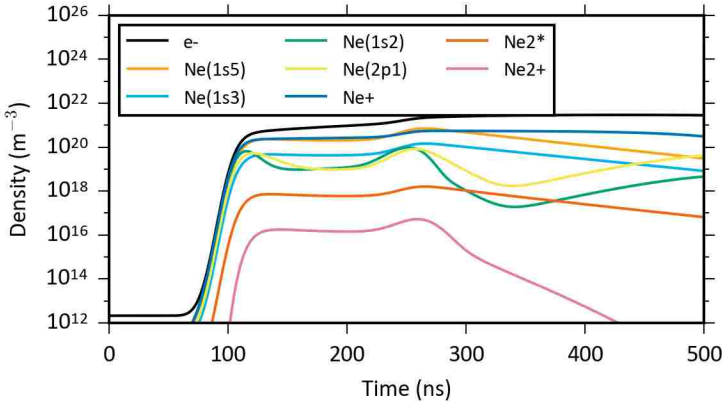

[redacted]

model is initialized with an ionization fraction of 10^{-13} representing a negligible amount of preionization. The electron density grows rapidly accompanied by the atomic states of neon. The neon excimer and molecular ion states take longer to populate owing to the prerequisite excited states of atomic neon. The post-pulse rise in Ne($1s_2$) and Ne($2p_1$) states can be attributed to the recombination of neon ions into excited neon states.

4.4.4. Spectral Emissions

Lastly, the global model is able to provide the time evolution of emissions from the discharge. These are shown in **Figure 4-4**. Several additional radiative transitions are tracked by the model as detailed in the reactions Table 4-1. Here the transitions plotted are those for which experimental data were available. For each transition, the values have been normalized to the amplitude of the first peak. It should be noted that the radiative transition rates used were those for *untrapped* emissions. In reality, the VUV emissions are all resonant radiation, which should be treated appropriately. However, given the complex geometry and unknown densities of atomic oxygen, hydrogen, and nitrogen in the volume between the discharge and the spectrometer window no accounting was made for this effect. In reality, trapping would be expected to increase the effective lifetime of the trapped states shifting the peaks of these emissions relative to untrapped transitions such as $Ne(2p_1) \rightarrow Ne(1s_2)$.

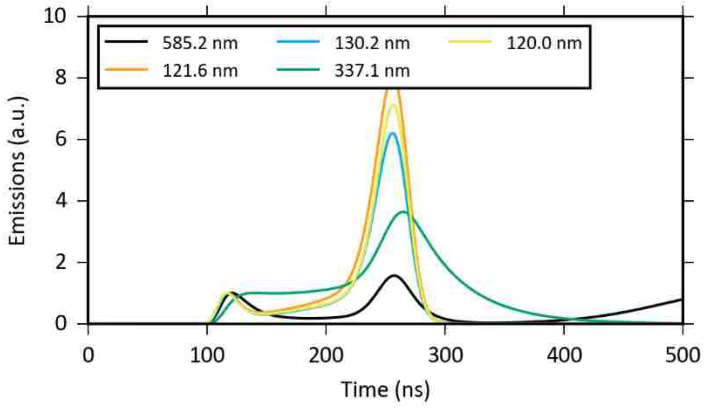

4.5. References

1. Yee, B.T. and R.P. Manginell, *Simple 0-D Model of a ns-pulsed Microdischarge in Atmosperic Pressure Neon.* In Preperation, 2017.

2. Chen, F., *Introduction to Plasma Physics and Controlled Fusion*. 2 ed. 1984, New York: Plenum Press.

3. Baalrud, S.D., J.D. Callen, and C.C. Hegna, *Instability-enhanced collisional effects and Langmuir's paradox.* Phys Rev Lett, 2009. **102**(24): p. 245005.

4. Kushner, M.J., *Modeling of microdischarge devices: Pyramidal structures.* Journal of Applied Physics, 2004. **95**(3): p. 846.

5. Kramida, A., Y. Ralchenk, J. Reader, and N.A. Team, *NIST Atomic Spectra Database* N.I.o.S.a. Technology, Editor. 2015: Gaithersburg, MD.

6. Itikawa, Y., *Cross sections for electron collisions with oxygen molecules.* Journal of Physical Chemistry Reference Data, 2009. **38**(1): p. 1-20.

7. Itikawa, Y., *Cross sections for electron collisions with nitrogen molecules.* Journal of Physical Chemistry Reference Data, 2006. **35**(1): p. 31-53.

8. Itikawa, Y. and A. Ichimura, *Cross sections for collisions of electrons and photons with atomic oxygen.* Journal of Physical Chemistry Reference Data, 1990. **37**(2): p. 637-651.

9. Yoon, J.-S., et al., *Cross sections for electron collisions with hydrogen molecules.* Journal of Physical and Chemical Reference Data, 2008. **37**(2): p. 913-931.

10. Wieser, J., et al., *Lyman-alpha emission via resonant energy transfer.* Atomic Molecular Optical Physics, 1998. **31**: p. 4589-4597.

11. Zatsarinny, O. and K. Bartschat, *Large-scale pseudostate calculations for electron scattering from neon atoms.* Physical Review A, 2012. **85**(6).

12. Sheverev, V.A., V.P. Stepaniuk, and G.G. Lister, *Chemi-ionization in neon plasma.* Journal of Applied Physics, 2002. **92**(7): p. 3454.

13. Akoshile, C.O., J.D. Clark, and A.J. Cunningham, *Reactions of excited neon atoms in neon-helium afterglows: I. Rate data.* Journal of Physics: B Atomic Molecular Physics, 1985. **18**: p. 2793-3803.

14. Rauf, S. and M.J. Kushner*Dynamics of a coplanar-electrode plasma display panel cell. I. Basic operation.* Journal of Applied Physics, 1999. **85**(7): p. 3460-3469.

15. Frommhold, L., M.A. Biondi, and F.J. Mehr, *Electron-Temperature Dependence of Electron-Ion Recombination in Neon.* Physical Review, 1968. **165**(1): p. 44-52.

16. Cohen, J.S. and B. Schneider, *Ground and excited states of Ne2 and Ne2+. I. Potential curves with and without spin–orbit coupling.* The Journal of Chemical Physics, 1974. **61**(8): p. 3230-3239.

17. Janev, R.K. and J.J. Smith, *Cross Sections for Collisions Processes of Hydrogen Atoms with Electrons, Protons and Multiply Charged Ions.* APID, 1993. **4**.

18. Baker, J., *Transition Probabilities for One Electron Atoms*, NIST, Editor. 2008: Washington D.C.

19. Tawara, H., et al., *Atomic Data Involving Hydrogens Relevant to Edge Plasmas.* Nagoya, 1986. **JP**.

20. Hibbert, A., E. Biémont, M. Godefroid, and N. Vaeck, *El transitions of astrophysical interest in neutral oxygen.* Journal of Physics B: Atomic, Molecular and Optical Physics, 1991. **24**: p. 3943-3958.

21. Cosby, P.C., *Electron–impact dissociation of oxygen.* The Journal of Chemical Physics, 1993. **98**(12): p. 9560-9569.

22. Kanik, I., et al., *Electron impact dissociative excitation of O 2 : 2. Absolute emission cross sections of the OI(130.4 nm) and OI(135.6 nm) lines.* Journal of Geophysical Research, 2003. **108**(11): p. 1-10.

23. Wang, Y., O. Zatsarinny, and K. Bartschat, *B-splineR-matrix-with-pseudostates calculations for electron-impact excitation and ionization of nitrogen.* Physical Review A, 2014. **89**(6).

24. Tachiev, G.I. and C.F. Fischer, *Breit-Pauli energy levels and transition rates for nitrogen-like and oxygen-like sequences.* Astronomy and Astrophysics, 2002. **385**(2): p. 716-723.

25. Valk, F., et al., *Measurement of collisional quenching rate of nitrogen states N2(C 3Πu,v= 0) and {\rm N}_2^+ (B\,^{\rm 2}\Sigma_{\rm g}^+,v=0).* Journal of Physics D: Applied Physics, 2010. **43**(38): p. 385202.

26. Gilmore, F.R., R.R. Laher, and P.J. Espy, *Franck–Condon Factors, r-Centroids, Electronic Transition Moments, and Einstein Coefficients for Many Nitrogen and Oxygen Band Systems.* Journal of Chemical Reference Data, 1992. **21**(5): p. 1005.

27. Märk, T.D. and H.J. Oskam, *Production and loss of N 2 + , Ne+ and Ne 2 + during the decay period of plasmas produced in neon-nitrogen mixtures.* Zeitschrift für Phys., 1971. **247**(1): p. 84-94.

28. Brom, J.M., J.H. Kolts, and D.W. Setser, *Quenching Rate Constants for Ne3(P2) Metastable Atoms at Room Temperature.* Chemical Physics Letters, 1978. **55**(1): p. 44-48.

29. Jones, E., T. Oliphant, and P. Peterson. *SciPy: Open Source Scientific Tools for Python*. 2001 08/20/2016]; Available from: http://www.scipy.org. .

30. Hairer, E., P. Norsett, and G. Wanner, *Solving Ordinary Differential Equations I. Nonstiff Problems*. 2nd ed. 1993: Springer-Verlag.

31. Becker, K.H., K.H. Schoenbach, and J.G. Eden, *Microplasmas and applications.* Journal of Physics D: Applied Physics, 2006. **39**(3): p. R55-R70.

32. Bolouki, N., K. Tomita, S. Hassaballa, Y. Yamagata, and K. Uchino, *Temporal evolution of electron density and electron temperature profiles in a non-thermal atmospheric-pressure plasma measured by laser Thomson scattering.* Japanese Journal of Applied Physics, 2015. **54**(1): p. 016101.

33. Dufour, T., *Etude expérimentale et simulation des micro-plasmas générés dans des micro-cathodes creuses* 2009, Université d'Orléans.

Chapter 5

Conclusion and Future Work

5.1 Conclusion

Exposure to hazardous chemicals affects more than 350,000 people per year globally [2, 3]. The current lack of universal and selective detection that is robust, portable, low energy, and accurate has lead to the investigation of plasma microdischarges as detectors. While laboratory results have been promising [4-7], field conditions add extra challenges such as carrier gas and detector gas contamination, which can lead to untrustworthy results, both in the form of false positives and false negatives.

An examination of common impurity gases that are likely to be experienced in the field application of microdischarge detectors and how they behave in an atmospheric pressure ns-pulsed Si-MHCD in Ne has been presented. Specific contaminants include N_2, N, H_2, H, H_2O and O. It was found to be likely that both H and O experienced resonant energy transfer with Ne excimers and that they competed in this reaction pathway. By increasing the O_2 concentration in our 0D model, we showed that the relative emissions of H (121.6 nm) dropped as the O emissions (130.2 nm) increased.

Further, we found that the O emission triplet centered at 130.2 nm was higher than expected based on the measured chamber concentrations and results from our 0D model. Combined with high levels of O_2 found on the surface of the Si cavity by EDS, we propose that O_2 is being concentrated in the chamber walls in the form of SiO_2 during ns-pulsed operation. This would lead to an increased O concentration in the discharge with respect to the bulk chamber gas. As a result, if the 121.6 nm Lyman-α is an important emission line used by a detector, the O_2 concentration must be carefully controlled.

Temporal ignition characteristics in the ns scale were examined to understand possible reaction dynamics. Species capable of resonant energy transfer with Ne excimers were found to emit predominantly during ignition and extinction, with flat emissions during the bulk of the pulse. On the other hand, emissions from states that benefitted from metastable formation, such as the N_2 molecule, increased as a function of time between ignition and extinction.

Device operation, lifetime, and failure modes were compared under DC and ns-pulsed DC driving conditions. An increase in device life of 6 times was achieved by operating in ns-pulsed mode at 10 kHz. Further, the radiant power of the DC discharge consistently fell during operation until the device catastrophically failed. The failure was attributed to development of a short between the top electrode and the dielectric Si cavity created by sputtering of the top Ni layer. The ns-pulsed discharge exhibited consistent operation for up to and hour, and then gradually began to experience transient extinction/ignition spikes within each pulse. By increasing the driving voltage, the measured current and voltage would stabilize for a time on the order of minutes until the transients would return, signifying an increase in the breakdown voltage, which we attributed to the development of an insulating SiO_2 surface oxide layer on the cavity walls. This further supports the need to control the gas O_2 concentration.

5.2 Future Work

In order to address device operative lifetime, Eden *et al* augmented their devices by deposited a Si_3N_4 layer [8]. With this approach, the stability, lifetime, and cavity-cavity uniformity of their MD were increased substantially. Briefly, prior to electrode deposition, a 2 μm thick silicon nitride film was grown in the Si cavity and over the aperture using low pressure vapor deposition. A dielectric Si dioxide or polyamide was then deposited only on the top surface, followed by the deposition of a 0.2 μm Ni electrode. Lastly, another 2 μm silicon nitride film was deposited, covering the cavity walls and top electrode. Figure 5-1 shows the finished inverted-pyramid design.

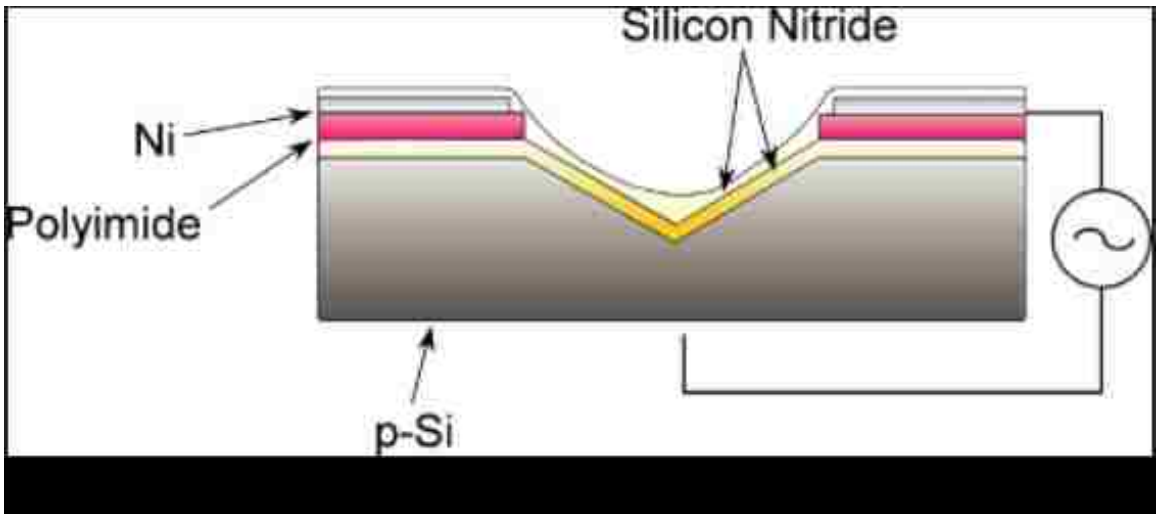

Using the same method, we propose to create new discharge arrays and reexamine the growth of a SiO_2 layer on the cavity wall and device life. Further, we will examine the impact of the same list of contaminants using a variety of chamber gases, including He, Ar, and air.

As a method to increase the selectivity of a PID detector, we will investigate the use of multiple discharge arrays with independent electrical driving conditions, which

may allow for the selective excitation and detection of chemical species based on their different ionization potentials [5]. As a result, species with similar size and affinity for a GC stationary phase that coelute, may be discriminated by the detector.

5.3 References

1. Eden, J.G., S.-J. Park, N.P. Ostrom, and K.-F. Chen, *Recent advances in microcavity plasma devices and arrays: a versatile photonic platform.* Journal of Physics D: Applied Physics, 2005. **38**(11).

2. Rocheleau, M., *Chemical Exposure Deaths on the Job Getting Rarer*, in *Boston Globe*. 2016: Boston.

3. *The World Health Report 2003 - Shaping the Future*. 2003, The World Health Organization: Geneva.

4. Miclea, M., et al., *Decomposition of Halogenated Molecules in a Micro-Structured Electrode Glow Discharge at Atmospheric Pressure*, in *Hakone VIII*. 2002: Puehajaerve, Estonia. p. 206.

5. Becker, K.H., K.H. Schoenbach, and J.G. Eden, *Microplasmas and applications.* Journal of Physics D: Applied Physics, 2006. **39**(3): p. R55-R70.

6. Narayanan, S., G. Rice, and M. Agah, *A micro-discharge photoionization detector for micro-gas chromatography.* Microchimica Acta, 2013. **181**(5-6): p. 493-499.

7. Zhu, H., et al., *Low-Power Miniaturized Helium Dielectric Barrier Discharge Photoionization Detectors for Highly Sensitive Vapor Detection.* Anal Chem, 2016. **88**(17): p. 8780-6.

8. Eden, J.G. and S.J. Park, *Microcavity plasma devices and arrays: a new realm of plasma physics and photonic applications.* Plasma Physics and Controlled Fusion, 2005. **47**(12B): p. B83-B92.